ARL-TR-9678 • Apr 2023

DEVCOM ARMY RESEARCH LABORATORY

Finite Element Modeling for Constitutive Property Determination from Instrumented Dynamic Spherical Indentation

by John D Clayton, Daniel T Casem, and Jeffrey T Lloyd

NOTICES

Disclaimers

The findings in this report are not to be construed as an official Department of the Army position unless so designated by other authorized documents.

Citation of manufacturer's or trade names does not constitute an official endorsement or approval of the use thereof.

Destroy this report when it is no longer needed. Do not return it to the originator.

ARL-TR-9678 ● APR 2023

Finite Element Modeling for Constitutive Property Determination from Instrumented Dynamic Spherical Indentation

John D Clayton, Daniel T Casem, and Jeffrey T Lloyd
DEVCOM Army Research Laboratory

REPORT DOCUMENTATION PAGE

Form Approved
OMB No. 0704-0188

PLEASE DO NOT RETURN YOUR FORM TO THE ABOVE ADDRESS.

1. REPORT DATE *(DD-MM-YYYY)*	**2. REPORT TYPE**	**3. DATES COVERED (From - To)**
April 2023	Technical Report	October 2022–March 2023

4. TITLE AND SUBTITLE
Finite Element Modeling for Constitutive Property Determination from Instrumented Dynamic Spherical Indentation

5a. CONTRACT NUMBER

5b. GRANT NUMBER

5c. PROGRAM ELEMENT NUMBER

6. AUTHOR(S)
John D Clayton, Daniel T Casem, and Jeffrey T Lloyd

5d. PROJECT NUMBER

5e. TASK NUMBER

5f. WORK UNIT NUMBER

7. PERFORMING ORGANIZATION NAME(S) AND ADDRESS(ES)
DEVCOM Army Research Laboratory
ATTN: FCDD-RLA-TB
Aberdeen Proving Ground, MD 21005-5066

8. PERFORMING ORGANIZATION REPORT NUMBER
ARL-TR-9678

9. SPONSORING/MONITORING AGENCY NAME(S) AND ADDRESS(ES)

10. SPONSOR/MONITOR'S ACRONYM(S)

11. SPONSOR/MONITOR'S REPORT NUMBER(S)

12. DISTRIBUTION/AVAILABILITY STATEMENT
Approved for public release; distribution is unlimited.

13. SUPPLEMENTARY NOTES
primary author's email: <john.d.clayton1.civ@army.mil>.

14. ABSTRACT
Finite element (FE) modeling of instrumented dynamic indentation experiments in a miniature Kolsky bar is undertaken. The test material is polycrystalline aluminum alloy Al 6061-T6. The FE model, with representative material parameters from the literature, accurately reproduces the curvature of the experimental load versus depth data for three different experimental indentation velocity histories. A framework for dimensional analysis of instrumented dynamic spherical indentation is set forth, improving upon prior work. Parametric FE simulations reveal sensitivities of the predicted response to variations in the proposed independent dimensionless variables encompassing material properties. Based on the dimensional analysis, static indentation and elevated temperature indentation are recommended for extraction of quasi-static and thermal properties from previously uncharacterized metals, and dynamic indentation is recommended for extraction of strain-rate sensitivity that cannot be obtained from static tests. Rate sensitivity obtained from the dynamic indentation experiments and simulations produces a parameterized stress-strain response for Al 6061-T6 reasonably validated by external studies for strain rates up to the order of 10^3/s.

15. SUBJECT TERMS
indentation, metals, plasticity, rate dependence, constitutive modeling, Johnson-Cook, Kolsky bar, Hopkinson bar

16. SECURITY CLASSIFICATION OF:			**17. LIMITATION OF ABSTRACT**	**18. NUMBER OF PAGES**	**19a. NAME OF RESPONSIBLE PERSON**
a. REPORT	**b. ABSTRACT**	**c. THIS PAGE**			John D Clayton
Unclassified	Unclassified	Unclassified	UU	78	**19b. TELEPHONE NUMBER (Include area code)** 410-278-6146

Standard Form 298 (Rev. 8/98)
Prescribed by ANSI Std. Z39.18

Contents

List of Figures

List of Tables

Acknowledgments

The authors acknowledge support from the intramural component of the High-Throughput Materials Discovery for Extreme Conditions program at the US Army Combat Capabilities Development Command Army Research Laboratory.

This report encompasses and extends research recently published in abbreviated form by the authors in a refereed article[1] in the *International Journal of Mechanical Sciences* (2023).

[1]Clayton J, Lloyd J, Casem D. Simulation and dimensional analysis of instrumented dynamic spherical indentation of ductile metals. International Journal of Mechanical Sciences. 2023;251:108333.

1. Introduction

A number of experimental techniques exist for characterizing the constitutive response of ductile elastic-plastic solids, including traditional tension, compression, and torsion experiments at low and high applied strain rates. Alternatively or simultaneously, indentation experiments can be used to ascertain properties of substrate materials via careful analysis of force-depth data, analysis of derived quantities such as indentation stress and strain,[1,2] and consideration of supplementary data such as size and shapes of residual imprints. Comparison of experimental data with numerical solutions obtained from FE simulations[3–6] facilitates the modern constitutive property extraction process, since exact analytical solutions are available only for very simple material behavior (e.g., linear elasticity) and since approximate solutions for more complex behavior are limited in scope and accuracy.[7] However, a disadvantage of the indentation experiment, relative to traditional methods that supply more uniform stress and strain fields over sampled material regions, is that stress and strain fields are highly nonuniform during indentation. Thus, even though indentation may be easier to perform and at lower cost, analysis of the data is more cumbersome.

Dynamic instrumented indentation is the focus of the present investigation. Unlike static indentation, dynamic indentation offers the possibility of characterization of the strain rate sensitivity of the material.[8–12] Furthermore, inertia and temperature changes under near-adiabatic conditions could affect results, the former especially at very high impact velocities.[13,14] In dynamic indentation, strain rate, like strain itself, is also highly nonuniform, even if the indenter's velocity is constant.[13] In any real experiment, the indenter will always decelerate prior to unloading.

Instrumented dynamic indentation using the split Hopkinson pressure bar (SHPB) (i.e., Kolsky bar), as often first credited to Subhash and co-workers,[15,16] has been invoked with a variety of indenter geometries and target materials. Instrumented dynamic indentation enables recording of velocities and mechanical forces during the transient indentation process for subsequent analysis. Recent methods with the SHPB have used a full sphere sandwiched between two specimens[17] or a striker with variable impedance to achieve load cycling.[18–20] Dynamic conical indentation experiments were used[9] to deduce strain rate sensitivity, where the indenter was propelled by a light gas gun, and a combination of interferometry and load transducer

was used to obtain a time-resolved response. A novel aspect of the current study, compared to other works that simulate instrumented dynamic indentation,[9,17,21] is the present use of a miniaturized SHPB rather than a full-scale system. Advantages of miniaturization include reduced inertial effects and decreased velocity rise times in the input and output bars.[20,22] Samples are generally smaller in size, and higher strain rates can be achieved through miniaturization, at least for conventional (uniform versus indentation) loading.[22]

The present research ultimately seeks to enable extraction of material constitutive properties from dynamic spherical indentation tests. The material description is restricted to classical ductile elastic-plastic solids[23,24] (e.g., engineering metals). Excluded from the present work are consideration of length scale and size effects.[25–27] The basic constitutive models considered here do not contain any intrinsic length scale(s).

Reviews of methods from the literature for material property extraction from static and dynamic indentation experiments and simulations are available in a preliminary report[28] and subsequent review article.[29] Also in those recent works,[28,29] the governing relationships among global variables were cast in dimensionless form in a new application of dimensional analysis to dynamic spherical indentation. In such dimensional analysis, the relationships among those dependent and independent variables deemed most useful are analyzed in the context of Buckingham's Pi theorem,[30–32] which has been applied elsewhere toward static spherical indentation[33] and dynamic projectile impact.[34] Buckingham's Pi theorem is used to systematically reduce the number of independent quantities. That work[28,29] notably extended the treatment of Lee and Komvopoulos[14] to account for thermal effects, and different mathematically admissible choices were made for dimensionless independent and dependent variables. See also the study of Nguyen et al.[35] that employs a different plastic constitutive law and a different set of dimensionless parameters for extraction of material properties from FE simulations of dual sharp and spherical indentation at relatively low but finite rates, again under isothermal conditions. In contrast to the current work, instrumented dynamic indentation data from SHPB testing were not reproduced in these prior simulations.[14,35]

Since the end goal of the present study is establishment of a combined experimental-numerical methodology to extract dynamic properties, some prior prominent works

on this topic are noted. Burley et al.[36] performed dynamic 5-mm-diameter spherical impact experiments and FE simulations on copper targets, with impact velocities ranging from 50 to 300 m/s. Strain rate sensitivity and frictional properties were obtained by a goodness-of-fit procedure on displacement-time histories and residual indent shapes. Characteristic strain rates ranged from 10^4 to 10^6/s, and temperature rises were significant enough to impart thermal softening. Ito et al.[11] performed dynamic FE simulations of ballistic impact of spheres into 10 different target metals to verify an analytical expression relating crater depth to strain rate sensitivity of flow stress. Impact velocities ranged from 0.6 to 180 m/s, and strain rates from 10^2 to 10^5/s. That method[11] for identification of rate sensitivity requires indentation depths attained from impacts at two distinct velocities. Lu et al.[9] used dynamic sharp indentation gas-gun experiments, verified by FE modeling, to obtain strain rate sensitivity of copper. Impact velocities ranged from 6 to 35 m/s and strain rates from 875 to 1750 m/s. Dynamic plasticity model parameters were obtained from simulations[37] of specimens in full-size Kolsky bar tests on steel in tension at rates from 500 to 1500/s; simulations of these and other full-scale Kolsky bar experiments at up to 3600/s were used to obtain dynamic properties for two steels.[38] Nguyen et al.[35,39] obtained yield, hardening, and rate sensitivity parameters for steels using indentation and FE modeling at lower strain rates ranging from 0.002 (quasi-static) to 0.4/s (low-rate dynamic).

In the current work, the dynamic dimensional analysis[14,28,29] is further refined to efficiently study effects of parameters entering the popular Johnson-Cook plasticity model.[23] This is one of the most widely used high-rate constitutive models for ductile metals because of its simplicity and containment of necessary physical ingredients to curve-fit experimental stress-strain data at different strain rates and temperatures. The current research directly models instrumented dynamic spherical indentation experiments in a miniature Kolsky bar apparatus, where the experiments were recently designed and implemented by Casem and coworkers.[18–20] The first stage of the investigation assesses suitability of the explicit dynamic FE code `ALE3D`[40] to reproduce the experimental test configuration and the data acquired from three different complex applied velocity histories, rather than constant indenter velocities, which are much more easily implemented numerically[13,14] but impossible to achieve in real experiments. To this end, accuracy of the Johnson-Cook model enters the procedure, where representative baseline properties from the literature[22,41–43] on the substrate material are used, without attempting calibration to

the current indentation data. The material of choice is a polycrystalline aluminum (Al) alloy designated Al 6061-T6. Mesh densities necessary for extraction of transient indentation force-depth and stress-strain data, the latter requiring the contact radius, are determined. Local field variables (e.g., stress, plastic strain, temperature) and global variables such as mean contact pressure are elucidated.

The second major stage of the current investigation establishes the framework for dimensional analysis and applies this framework to systematically investigate relative effects of constitutive parameters (as well as initial temperature) on the predicted dynamic indentation response. Results show which parameters may be reasonably expected to influence indentation force-depth data, and thus are candidates for extraction via calibration of FE solutions to experiments. Implementation of such calibration methods, which likely requires sophisticated numerical optimization strategies (e.g., machine learning techniques[6,44] for accuracy, speed, and stability) as well as analysis of uniqueness of inverse solutions,[35,45,46] is outside the scope of the present study.

The third and final stage of this investigation demonstrates successful extraction of the strain-rate sensitivity parameter from experimental data and parametric FE simulations. An error measure associated with cumulative work of indentation is defined and minimized for parameter optimization. Stress-strain predictions of the constitutive model and parameter set are compared versus those obtained from external studies that used conventional static and dynamic methods (e.g., standard SHPB) and are also validated versus static experimental indentation data from an independent external source.

Sections of this report include the following content. Fundamentals of indentation analysis, both static and dynamic, and corresponding generic constitutive models are presented in Section 2. Experiments[20,29] are described briefly in Section 3, followed by more extensive details of the FE model with baseline parameters. This FE model has not been presented elsewhere with the exception of the complementary journal article[47] that abbreviates this report. Results of Section 3 reveal both success and limitations of the baseline model for reproducing certain features observed in data from three instrumented dynamic tests. The dimensional analysis and sensitivity investigation are discussed in Section 4, including proposed experimental methods for extraction of parameters for previously uncharacterized ductile met-

als. Extraction of strain rate sensitivity and parameter comparisons are presented in Section 5. Conclusions follow in Section 6. Exploratory simulations including much higher loading rates are contained in the appendix.

2. Fundamentals

Methods of analysis of indentation and general forms of inelastic constitutive models are summarized in Section 2. The static case is addressed first, for elastic and then elastic-plastic solids, followed by the dynamic case. Measures of indentation stress and strain are defined. The focus is on governing equations used for subsequent applications to spherical indentation in Sections 3, 4, and 5; more thorough treatments are available elsewhere (e.g., Johnson[7]).

2.1 Static Elastic Indentation

The elastic solutions of Hertz are often used to analyze static indentation up to initial yield, as well as elastic unloading from a plastically deformed state. The Hertz analysis[7] assumes frictionless contact of homogeneous elastic bodies whose surfaces are parabolic in shape. The constitutive model is isotropic and linear elastic. Hertz's equations for spherical indentation into an initially flat substrate are expressed as follows.[7,48] Indicate by P the indentation force, h_e the elastic (i.e., reversible) indentation depth, $\bar{E}$ the effective system modulus, $\bar{R}$ the effective system radius, a the contact radius, and $\bar{k}$ a system stiffness. Let $E_i, E_s, \nu_i, \nu_s, R_i, R_s$ be the elastic moduli, Poisson's ratios, and radii, labeled with respective subscripts $(\cdot)_i$ and $(\cdot)_s$ for indenter and substrate. Then

$$P = \bar{k} h_e^{3/2}, \qquad \bar{k} = \tfrac{4}{3}\bar{E}\bar{R}^{1/2}, \qquad a = (\bar{R}h_e)^{1/2}; \tag{1}$$

$$\bar{E} = [(1-\nu_i^2)/E_i + (1-\nu_s^2)/E_s)]^{-1}, \qquad \bar{R} = (1/R_i + 1/R_s)^{-1}. \tag{2}$$

Before deformation, $R_s \to \infty \Rightarrow \bar{R} = R_i$. Often, $R_s \to \infty$ and R_i =constant (i.e., small deformation theory) are used to approximate the entire elastic loading process of a stiff indenter into a flat substrate, which produces a very simple closed-form solution. The same approximations are also often used to analyze elastic unloading[49]; however, unloading from a plastic impression has also been described with a finite R_s.[50]

For a rigid indenter, $\bar{E} = E_s/(1-\nu_s^2)$ and $R_i =$ constant. On the other hand, if the

indenter is deformable, its elastic displacement h_i can be approximated by Hertz's solution for indentation into a rigid flat surface[48]:

$$h_i \approx 3(1-\nu_i^2)P/(4E_i a). \tag{3}$$

The effective system modulus $\bar{E}$ fully contains effects of material constitutive behavior on the load-displacement curves in the linear elastic regime. This modulus has also been used to encompass all *elastic* constitutive effects on load-displacement response in the elastic-plastic regime of indentation,[45] as justified by some analytical and numerical solutions.[4,7,51]

2.2 Static Elastic-Plastic Indentation

In the elastic-plastic regime, the elastic indentation depth of the system is labeled as h_e, and the residual indentation depth is written as h_r. The contribution of the deformation of the indenter to the total depth is written as h_i, with h_s the remainder. Then, the total depth h is decomposed into the sums[48]

$$h = h_e + h_r = h_s + h_i; \qquad h_e = (P/\bar{k})^{2/3}. \tag{4}$$

If the indenter deforms only elastically, as is typically the case for a very strong and stiff indenter, then h_i can be approximated from Eq. 3. After elastic unloading, $h = h_r$ and $h_e = h_i = 0$. During elastic unloading, the force-depth curve has a slope S suggested from Hertz's theory of[29]

$$S(h_e, h_r) = \partial P(h_e, h_r)/\partial h_e = \tfrac{2}{3}\bar{k}(h_r) \cdot h_e^{1/2} = 2\bar{E} \cdot a(h_e, h_r). \tag{5}$$

The contact radius a at depth h can be inferred from Eq. 5 when S is measured at a given elastic-plastic contact depth h, if $\bar{E}$ is known from independent measurements.[52] The radius of the residual indent (i.e., crater) after unloading, denoted by a_r, of a plastically deformed material has been widely used to approximate a at peak load for various indenter geometries,[49] though more sophisticated treatments of unloading of elastic-plastic solids exist.[50]

Constitutive behavior of isotropic ductile metals is described in traditional engineering practice via isotropic elasto-plasticity with possible power-law hardening.[6,44,45,53,54] Denote the cumulative scalar plastic strain by ϵ^P, the initial yield stress by σ_0, the strain hardening exponent by n, and a hardening coefficient by κ. Then a standard

model for von Mises-equivalent flow stress σ under isothermal conditions is

$$\sigma(\epsilon^P) = \sigma_0 \left[1 + \kappa \cdot (\epsilon^P)^n\right], \qquad n = \mathrm{d}\ln(\sigma - \sigma_0)/\mathrm{d}\ln\epsilon^P. \tag{6}$$

For perfect plasticity, $\kappa = 0$, and for linear hardening, $n = 1$ with $\kappa > 0$. Established methods (i.e., associative flow, normality, consistency) are used to implement Eq. 6 in the context of finite deformations with incremental plasticity in numerical settings[24] (e.g., FE software for solid mechanics):

$$\mathrm{d}\boldsymbol{\epsilon} = \mathrm{d}\boldsymbol{\epsilon}^E + \mathrm{d}\boldsymbol{\epsilon}^P, \qquad \mathrm{d}w^P = \boldsymbol{\sigma} : \mathrm{d}\boldsymbol{\epsilon}^P = \sigma\,\mathrm{d}\epsilon^P. \tag{7}$$

The tensor-valued strain increment $\mathrm{d}\boldsymbol{\epsilon}$ is decomposed into an elastic $(\cdot)^E$ and plastic $(\cdot)^P$ part, the Cauchy stress tensor is $\boldsymbol{\sigma}$, and the non-negative scalar plastic strain increment $\mathrm{d}\epsilon^P$ is found from the increment of the plastic strain tensor under the requirement that its work conjugate entering plastic work per unit volume w^P is the von Mises stress σ. For uniaxial stress conditions,

$$\sigma = \begin{cases} E\epsilon & (\epsilon \leq \sigma_0/E), \\ \sigma_0 \left[1 + \kappa \cdot (\epsilon^P)^n\right] & (\epsilon \geq \sigma_0/E). \end{cases} \tag{8}$$

Here ϵ is the total axial strain and σ the axial stress, in this context equal to the von Mises stress.

2.3 Dynamic Indentation

Dynamics introduces several complexities not present in static indentation. In addition to mechanisms pertinent to quasi-static indentation (i.e., elasticity, yield, and strain hardening), rate dependent dislocation kinetics manifests as strain rate sensitivity, usually increasing the plastic flow resistance as strain rate increases. Stress wave propagation, which involves mass density ρ_0, enters the dynamic problem. For loading times short relative to the time required for heat transport, deformation conditions can be approximated as adiabatic and temperature rise could be non-negligible, so specific heat capacity (e.g., c_V) may also affect the response. Finally, dislocation kinetic processes depend on loading rate to varying degrees, depending on the specific metallic material. Impact conditions are not severe enough for problems studied in the present experimental conditions to necessitate inclusion of nonlinear elasticity (e.g., pressure-dependent compressibility) or thermoelastic cou-

pling (i.e., thermal expansion), which would be required to describe intense shock waves, for example.[55] Ballistic rates of loading considered in the appendix, however, do warrant consideration of thermoelastic and nonlinear elastic effects.

For isotropic ductile polycrystalline metals, the inelastic constitutive model of Eq. 6 is usually extended to dynamic regimes by allowing for strain rate and thermal effects, in addition to initial yield and strain hardening. A generic form of flow stress is a product of terms accounting for each mechanism:

$$\sigma(\epsilon^P, \dot{\epsilon}^P, T) = \sigma_0 \left[1 + \kappa \cdot (\epsilon^P)^n\right] \cdot f(\dot{\epsilon}^P) \cdot g(T). \tag{9}$$

Functions f and g account, respectively, for strain rate and thermal sensitivity. Denoted by T is absolute temperature and by $\dot{\epsilon}^P$ the scalar effective plastic strain rate such that $\mathrm{d}\epsilon^P = \dot{\epsilon}^P \mathrm{d}t$ over time increment $\mathrm{d}t$.[24] In rate form, Eq. 7 becomes, with $\dot{\boldsymbol{\epsilon}}$ the Eulerian velocity gradient[56] and $\dot{w}^P$ the local rate of plastic working per unit current volume,

$$\dot{\boldsymbol{\epsilon}} = \dot{\boldsymbol{\epsilon}}^E + \dot{\boldsymbol{\epsilon}}^P, \qquad \dot{w}^P = \boldsymbol{\sigma} : \dot{\boldsymbol{\epsilon}}^P = \sigma\, \dot{\epsilon}^P. \tag{10}$$

The local temperature rate is found from the continuum balance of energy,[56] where notation c_V is specific heat at constant volume per unit reference volume and ρ the current mass density:

$$(\rho/\rho_0) c_V \dot{T} \approx \zeta \cdot \dot{w}^P \approx \zeta \cdot \sigma\, \dot{\epsilon}^P. \tag{11}$$

Thermoelastic coupling is omitted with adiabatic conditions assumed in Eq. 11. The Taylor-Quinney factor is $\zeta \in [0, 1]$, usually closer to unity than zero and usually assumed constant in standard FE software, though ζ often more realistically evolves with plastic deformation.[57,58]

2.4 Indentation Stress and Strain

Correlation of the loading portion of a predicted force-displacement curve with test data[3] has been used to determine quasi-static plasticity parameters (e.g., σ_0, κ, n), and unloading used to determine elastic stiffness $\bar{E}$ given some estimate of the contact area.[49,50] Periodic load-unload cycles can alternatively reveal the projected contact area πa^2 if $\bar{E}$ is measured from the initial elastic loading phase.[1]

Denote the mean contact pressure by p, often identified with Meyer's hardness H

in a Brinell test:

$$p = P/(\pi a^2) = H \approx c\bar{\sigma}. \tag{12}$$

The effective flow stress σ in the sample is $\bar{\sigma}$, and c is the constraint factor that generally depends on geometry and constitutive behavior.[3,50,59,60] Yielding begins at $c \approx 1.1$,[50,59] whereby h_p first becomes nonzero. For deep indentation, $h \gg h_e$ so the plastic response dominates. In this regime, the historical analysis and data of Tabor[61] suggest $c \approx 2.8$ for spherical indentation of ductile metals, corroborated by numerical methods.[62] Another typical approximation is $c \approx 3$ for this deep plastic regime.[50] Between elastic and deep plastic indentation, $1.1 \lesssim c \lesssim 3$.

For strain hardening materials ($n > 0$), c should depend on both n and the choice of "indentation strain" substituted into Eq. 8 for ϵ^P to acquire a representative value of $\bar{\sigma}$.[3,50] Tabor[61] proposed $\epsilon^P \approx \bar{\epsilon}$, where

$$\bar{\epsilon} = 0.2a/R_i, \tag{13}$$

which corresponds to plastic strain at the indentation edge.[3] Tabor[61] assumed $a \approx a_r$ for the contact radius at maximum load, where the radius a_r is that of the residual indent after load removal. This assumption is inconsistent with the Hertz definition of the true contact area at the instant load removal begins, though it may still be accurate in some cases.[49]

Definitions of indentation strain[2,50,61] often incorporate the contact radius a, which may be challenging to obtain directly from experiments. An estimate proposed by Field and Swain[50] is

$$a = [2(h - h_e/2)R_i - (h - h_e/2)^2]^{1/2}. \tag{14}$$

However, noted by Kalidindi and Pathak,[1] the definition of a in Eq. 14—based on spherical geometry and assuming that the elastic displacement of a preformed spherical impression is evenly divided above and below the circle of contact[50]—is not fully consistent with Hertz's form Eq. 1. A strategy advocated by Pathak, Kalidindi, and their coworkers[2,6,53] compares indentation stress-strain curves rather than indentation force-displacement curves to ascertain elastic-plastic properties. The indentation stress-strain fitting method can be advantageous over fitting of force-displacement because elastic-plastic properties may be strongly correlated to

only small regions of the entire force-displacement curve.[44] Correlation of total and recoverable strain energies (i.e., integrals of load-displacement relations) may also be advantageous for property estimation, since integral values are less sensitive to experimental noise.[32,33]

An alternative measure of indentation strain $\hat{\epsilon}$, with corresponding renamed stress (i.e., mean pressure) $\hat{\sigma}$, as established by Kalidindi and Pathak,[1,2] is

$$\hat{\epsilon} = \frac{4}{3\pi}\frac{h_s}{a} \approx \frac{h_s}{2.4a}, \qquad \hat{\sigma} = p = \frac{P}{\pi a^2} \approx c\bar{\sigma}. \tag{15}$$

The contact radius obeys the Hertz definition in Eq. 1. This radius can be found from Eq. 5 during unloading if $\bar{E}$ is known from data collected in the elastic regime.[1,2] Note that Eq. 15 produces $\hat{\sigma} = \bar{E}\hat{\epsilon}$ for $h = h_e$, that is, for elastic loading/unloading commensurate with Hertz's solution in Eqs. 1 and 2. Use of Eq. 15 with experimental[48] and numerical[6,53] results gives $c \approx 2$ for perfectly plastic metals or for strain-hardening metals at a uniaxial-equivalent offset of $\epsilon \approx 0.1\% - 0.2\%$.

The procedures for producing uniaxial equivalent stress-strain curves from indentation stress and strain, where the latter are given by Eq. 15, are described by Patel and Kalidindi.[53] The equivalent scalar uniaxial stress-strain law for the specimen is $\sigma = E_s \cdot \epsilon^E = E_s \cdot (\epsilon - \epsilon^P)$. Then the following correspondence relations are derived among indentation stress-strain curves ($\hat{\sigma}$ vs. $\hat{\epsilon}$) and uniaxial curves (σ vs. ϵ)[28,29]:

$$\hat{\sigma} = \begin{cases} \bar{E} \cdot \hat{\epsilon} & (\hat{\sigma} \leq c\sigma_0), \\ \bar{E} \cdot (\hat{\epsilon} - \hat{\epsilon}^P) & (\hat{\sigma} \geq c\sigma_0); \end{cases} \qquad \hat{\epsilon} = \frac{4}{3\pi}\frac{h_s}{a} = \hat{\epsilon}^E + \hat{\epsilon}^P; \tag{16}$$

$$\epsilon^E = \frac{1}{c}\frac{E_s}{\bar{E}} \cdot \hat{\epsilon}^E = \frac{1}{c}\frac{E_s}{\bar{E}} \cdot \frac{\hat{\sigma}}{\bar{E}} = \frac{1}{c}\frac{E_s}{\bar{E}^2}\frac{P}{\pi a^2}, \qquad \epsilon^P = \frac{\hat{\epsilon} - \hat{\epsilon}^E}{\hat{\beta}}. \tag{17}$$

The constraint factor c is measured at $\bar{\sigma} = \sigma_0$, and $\hat{\beta}$ is a fitted parameter. For representative elastic-plastic solids with null or linear strain hardening, $c \approx 2.0 - 2.2$ and $\hat{\beta} \approx 1.3$.[53]

Dynamics introduces further complexity since strain rates are important. When comparing dynamic indentation data to experimental data that have been recorded at a less fluctuating rate (e.g., recorded from traditional Kolsky bar experiments), a measure of global or effective strain rate for the indentation experiment is often sought. Strain rates within the substrate are not constant in space or time domains.

Different definitions of indentation strain rate, and their applicability to instrumented dynamic spherical indentation data, have been reviewed in recent work.[28,29]

3. Finite Element Simulations of Indentation Experiments

3.1 Experimental Protocols

Experimental methods have been discussed by Casem[18–20] and are summarized in what follows. A miniature Kolsky bar (i.e., SHPB)[22] is adapted for instrumented dynamic spherical indentation. Transient force, displacement, and velocity data are acquired or inferred from each experiment. The loading history (e.g., indenter's velocity) depends on the velocity of the striker bar and geometric properties of the system (including pulse shaping) as well as indentation resistance due to properties of the substrate. Initial clearance between indenter and substrate also affects the velocity history. The loading history is thus not strictly controlled; however, different final indentation depths are generally achieved by increasing the striker velocity, which tends to increase the average loading rate. The duration of the loading pulse is dictated by the time required for a longitudinal wave to traverse twice the length of the striker bar. With the duration thus relatively fixed by the geometry, a greater final depth is attained by a larger striker velocity.

The system is shown schematically in Fig. 1 with a truncated input bar; the identical geometry is used for FE simulations. This view only contains the upper half of the system, which is axially symmetric. The system consists of a steel (4340) input bar, the Al 6061-T6 specimen (i.e., substrate), and a tungsten carbide (WC) output bar, all of nominally cylindrical shape with dimensions listed in Fig. 1. The spherical surface of the indenter is machined directly into the (right) end of the output bar. The radius of the cylindrical output bar is only $\frac{1}{4}$ the radius of curvature of its spherical tip, meaning the full hemispherical shape indenter is truncated. However, the contact region remains spherical throughout each experiment, that is, the truncation of the spherical tip does not affect results apart from possible wave interaction effects, later revealed to be negligible. The (right, not indented) face of the specimen is glued to the (left) end of the input bar.

The velocity history $v(t)$ of the input bar corresponding to its right side in Fig. 1 is obtained from analysis of diagnostic output of a strain gage. Histories are shown in Fig. 2a for each of three representative experiments, labeled tests 1, 2, and 3.

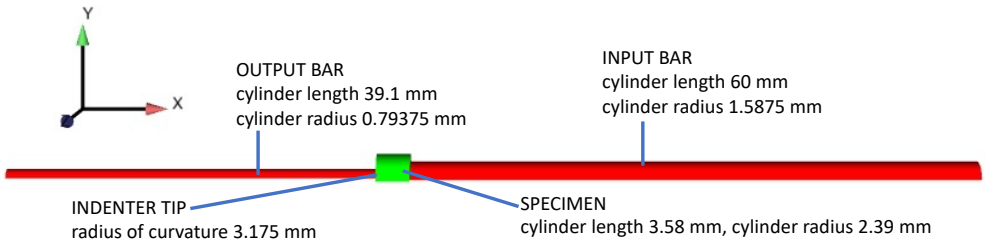

Fig. 1 Kolsky bar set-up: experimental data are extracted from NDI at the left end of the output bar and at the left end of the specimen (i.e., indented surface), and from a strain gage at the right end of the truncated input bar

The average velocity over the duration of each test is defined as follows, with t_f the end time beyond which $v \approx 0$, specifically 81 μs, 50 μs, and 60 μs for respective tests 1, 2, and 3:

$$\bar{v} = \frac{1}{t_f} \int_0^{t_f} v(t) \mathrm{d}t. \tag{18}$$

Because of finite wave speeds, the times at which loading and unloading occur in the indented sample do not match the times at which $\bar{v}$ changes in the input bar: absolute times for loading and unloading in the sample are shifted.

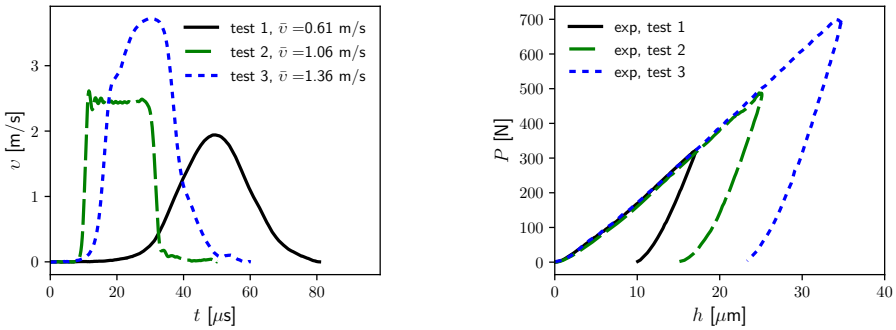

(a) input bar velocity (b) force vs. depth

Fig. 2 Experimental data: (a) inferred velocity history at truncated right end of input bar with average input velocity $\bar{v}$ for three tests (b) measured force P vs. depth h for three tests

Displacement histories of the indented face of the sample at its radial edge (left end) and the left end of the output bar are measured in-situ using a normal displacement interferometer (NDI) focused on each location. The displacement and force histories for the tip of the indenter, that is, the output bar at its right end in Fig. 1, are calculated using a linear elastic wave analysis with the strain gage and NDI data. Indentation depth h is defined as the difference between the indenter tip displacement and the radial edge displacement of the face of the substrate recorded by the NDI.

Unlike traditional static indentation, rigid body motion (translation) of both the indenter and specimen can be substantial. Deformations of the input and output bars remain elastic and small throughout the duration of each test; these components are thus reusable. All experiments reported here are performed at room temperature $T_0 \approx 300$ K.

Experimentally procured data include the loading and unloading force-displacement histories for each test shown in Fig. 2b. Certain results are summarized in Table 1 for reference, to be compared with numerical predictions later. Maximum load P_m and corresponding depth h_m increase with test number. Similarly, the residual imprint depth h_r and radius a_r also increase with test number. The residual imprint radius is measured using confocal microscopy.

The initial indenter radius is hereafter simply denoted as $R = R_i = 3.175$ mm. The initial sample dimensions are denoted by $L_s/D_s = \frac{3}{4}$ and $D_s = \frac{3}{2}R$. Static spherical indentation experiments on Al 6061-T6 have been reported elsewhere[6] with a WC indenter of radius $2R$. Finite element simulations of the static problem[6] to comparable indentation strains suggest that the radius and length of cylindrical specimens used in the current work are large enough to mitigate boundary edge effects for slow enough loading. Stress wave interactions with finite sample boundaries could have effects that cannot be ruled out a priori in dynamic experiments.

The measured indentation depth and depth rate are the respective true indentation depth h_s and depth rate $\dot{h}_s$ in the substrate, relative to those measured for the far-field surface away from any pile-up or sink-in effects. In Section 3 and Section 4, the notation is simplified such that $h_s \rightarrow h$ and $\dot{h}_s \rightarrow \dot{h}$. The elastic stiffness of WC ($E_i = 629$ GPa) is about an order of magnitude larger than that of aluminum. The approximation in Eq. 3 then suggests that the deformation of the spherical end of the indenter, h_i, should be negligible relative to h for loads and contact radii encountered in this work.

The substrate material is assumed homogeneous and isotropic. Analysis of static indentation[48] for the same Al 6061-T6 alloy, which has a mean grain diameter of 59 μm, suggests that the region of amply deformed material at the yield point for the current indenter radius contains 40 to 50 grains, enough to average out elastic and slip system anisotropies of individual crystals. Halving R to 1.6 mm would reduce the deformed volume by a multiplier of $\frac{1}{8}$, so only 5 to 7 grains would be sampled.

Thus, use of a much smaller indenter would invalidate the assumptions of material homogeneity and isotropy, and a single crystal plasticity model[58] should be used to resolve individual grains in simulations with small R.

3.2 Model Protocols

Dynamic FE simulations were conducted with the `ALE3D` code. Although the geometry is axisymmetric, a three-dimensional (3-D) rendering was found necessary to provide better contact stability. A quarter section of the true 3-D geometry, with appropriate symmetry boundary conditions on faces of symmetry, was sufficient; see Fig. 1 and Fig. 3. Hexahedral elements with reduced integration were employed. Meshes of the sample and proximal ends of input and output bars, the latter encompassing the indenter's tungsten carbide tip, are shown in Fig. 3.

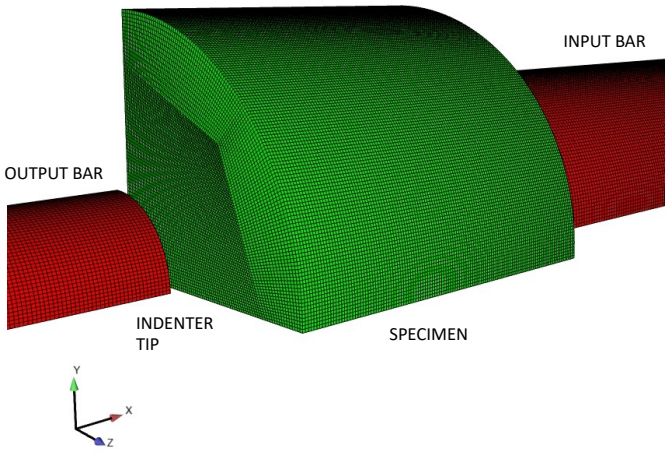

Fig. 3 Finite element mesh zoomed in on specimen, moderate mesh refinement ($3,092,480 \approx 3.1$**M total elements for entire system**)

Velocity history boundary conditions were applied to the end of the steel input bar, corresponding exactly to the three experimentally inferred velocity histories in Fig. 2a for tests 1, 2, and 3. As shown in the rightmost columns of Table 1, these input velocities lead to average indentation depth rates of around 1 to 3 m/s, and to average indentation strain rates ranging from around 1100/s to 2600/s depending on the definition used for indentation strain. In the appendix, lower and much higher velocities are investigated, with $\bar{v}$ multiplied up to tenfold.

Tied contact was used to model the glued interface between one face of the specimen and the input bar. Sliding separable contact with possible friction was used to model the interaction between indenter and the other face of the specimen. Adia-

batic conditions are invoked since analysis times are on the order of tens of μs: all plastic work is converted to thermal energy leading to local temperature rise.

Standard output from FE simulations includes transient nodal positions (e.g., giving deformed shapes) and local stress, plastic strain, and temperature fields. Such local fields cannot be obtained from experimental data. Global variables interrogated from simulations include the total indentation force P obtained from summing pertinent nodal forces, the indentation depth h measured as the difference between the displacement of the indenter tip and the radial edge of the specimen (similarly to experiments), and the transient contact radius a. To determine the latter, which is also not presently available from experiments, a small force threshold was used to delineate those nodes on the surface of the sample in direct contact with the indenter.

Deformations remained very small and elastic in the input and output bars throughout each simulation. Accordingly, only the mass densities and linear elastic moduli are important for the constitutive responses of the input bar (steel, $\rho_0 = 7.81$ g/cm^3, $E = 207$ GPa, $\nu = 0.29$) and output bar/indenter (WC, $\rho_0 = 14.9$ g/cm^3, $E = 629$ GPa, $\nu = 0.24$).

The substrate, consisting of polycrystalline Al 6061-T6, deforms plastically during the dynamic indentation process. The popular Johnson-Cook model[23,63] is invoked for the specific versions of yield and flow functions expressed generically in Eqs. 6 and 9:

$$\sigma(\epsilon^P, \dot{\epsilon}^P, T) = [A + B(\epsilon^P)^n] \cdot [1 + C \cdot \ln\{\dot{\epsilon}^P/\dot{\epsilon}_0\}] \cdot [1 - \{(T - T_R)/(T_M - T_R)\}^m]; \tag{19}$$

$$\sigma_0 = A, \quad \kappa = B/A; \qquad f = 1 + C \cdot \ln[\dot{\epsilon}^P/\dot{\epsilon}_0], \quad g = 1 - [(T - T_R)/(T_M - T_R)]^m. \tag{20}$$

In rate sensitivity function f of Eq. 20, $C = \partial\sigma/\partial \ln \dot{\epsilon}^P$ is a fitting parameter and $\dot{\epsilon}_0$ is a normalization constant. In g of Eq. 20, T_R and T_M are a reference temperature and melt temperature, with m a thermal softening exponent. When $T < T_R$, g is instead set to unity, which avoids numerical issues when $m < 1$, and when $T > T_M$, $g = 0$ since negative flow stress is prohibited. Usually, $B > 0$, $n > 0$, $C > 0$, and $m > 0$, such that strength increases with increasing strain and strain rate and decreasing temperature. Increasing n does not necessarily increase instantaneous yield strength, since ϵ^P is often less than unity. Since $T < T_M$ for solid behavior,

the smaller the value of positive m, the greater the strength decrement. On the other hand, flow stress for $\dot{\epsilon}^P > \dot{\epsilon}_0$ always increases with increasing C. Typically, and in the current work, $T_R < T_M$ and $\dot{\epsilon}_0 > 0$ are interpreted as fixed universal constants for normalization. Thus, the number of material parameters that may vary from material to material in Eq. 19 is six: A, B, C, m, n, T_M. Additionally, parameters that may vary with substrate material in the present context are the isentropic elastic moduli E, ν, specific heat per unit reference volume c_V, and mass density per unit reference volume ρ_0.

Trial simulations with thermal expansion and nonlinear compressibility enabled for the aluminum alloy showed that effects of thermal expansion from adiabatic temperature rise and effects of nonlinear compressibility were negligible for the present moderate loading rates. Thus, thermal expansion was disabled and constant bulk and shear moduli were used. The fixed Taylor-Quinney approximation $\zeta = 1$ was used in Eq. 11, presumably producing an upper bound on adiabatic temperature rise from plastic dissipation. As discussed later in Section 3.3, effects of static and dynamic friction at the contact surface (byproducts of properties of indenter and sample) were negligible on force-depth predictions for realistic values of corresponding coefficients, so contact friction was omitted in most simulations.

Relevant properties and parameters are listed in Table 2 with supporting references appended to the title. Variations among Johnson-Cook parameters exist in the literature for the same Al 6061-T6 material, depending on which experimental data and testing regimes are emphasized in the calibration procedure. Representative values based on the collective literature[22,40–42,64] are used here, to be refined in Section 5 on dynamic property extraction. All current simulations are performed at an initial temperature equal to the reference temperature: $T_0 = T_R$, in agreement with experimental protocols for tests 1, 2, and 3. Later in Section 4, T_0 is increased among some simulations to better elucidate effects of thermal softening. In these later simulations, thermal expansion is also omitted to avoid spurious contact interactions in the initial state, presuming that the experimental apparatus would be recalibrated at high temperature to account for any difference in sample dimensions due to thermal expansion. Property ranges investigated parametrically later are shown in Table 3.

Table 1 Loading conditions and results: average input velocity $\bar{v}$, force and depth at maximum load P_m and h_m, and residual imprint depth and radius h_r and a_r for experiments (exp) and simulations (sim); peak indentation strains $\bar{\epsilon}_m, \hat{\epsilon}_m$ and their average rates over the loading phase for simulations (experimental strains not available without measured a); average depth rates $\dot{h}_A$ (sim)

Test	$\bar{v}$ (m/s) (exp = sim)	P_m (N) (exp)	P_m (N) (sim)	h_m (μm) (exp)	h_m (μm) (sim)	h_r (μm) (exp)	h_r (μm) (sim)	a_r (μm) (exp)	a_r (μm) (sim)	$\bar{\epsilon}_m$ (-) (sim)	$\hat{\epsilon}_m$ (-) (sim)	$\dot{\bar{\epsilon}}$ (1/s) (sim)	$\dot{\hat{\epsilon}}$ (1/s) (sim)	$\dot{h}_A$ (m/s) (sim)
1	0.61	323	327	17.1	18.8	10.1	11.1	351	370	0.0202	0.0248	1100	1350	1.02
2	1.06	487	514	25.0	26.8	15.1	16.7	419	450	0.0245	0.0293	1898	2270	2.08
3	1.36	700	749	34.0	36.2	23.3	24.1	483	550	0.0287	0.0337	2223	2607	2.80

Table 2 Baseline geometric and material parameters[22,40,40–43,48,64]

Parameter (units)	Value	Definition	Parameter (units)	Value	Definition
E (GPa)	71.0	modulus of Al 6061-T6	ν (-)	0.33	Poisson's ratio of Al 6061-T6
ρ_0 (g/cm^3)	2.77	mass density of Al 6061-T6	c_V (MPa/K)	2.48	specific heat of Al 6061-T6
A (GPa)	0.3	initial yield strength of Al 6061-T6	B (GPa)	0.2	hardening coefficient of Al 6061-T6
n (-)	0.3	hardening exponent of Al 6061-T6	C (-)	0.05	rate sensitivity of Al 6061-T6
T_M (K)	925	melt temperature of Al 6061-T6	T_R (K)	300	reference temperature (universal)
m (-)	1	thermal softening of Al 6061-T6	$\dot{\epsilon}_0$ (1/s)	1	reference strain rate (universal)
$\bar{E}$ (GPa)	71.2	system modulus with WC indenter	R (mm)	3.175	indenter radius

Table 3 Ranges of dimensionless parameters of substrate investigated in simulations. Fixed components remain constant while dimensionless ratios are adjusted among simulations. Velocity boundary conditions and $\bar{v}$ correspond to test 3.

Dimensionless parameter	Values considered	Baseline	Fixed components	Description
E/E_0	0.2, 0.5, 1, 2, 10	1	$E_0 = 71$ GPa	elastic modulus*
ν	0, 0.15, 0.33, 0.45, 0.49	0.33	-	Poisson's ratio
$C_l/\bar{v} = \sqrt{E/\rho_0}/\bar{v}$	10^3, 2×10^3, 3.7×10^3, 5×10^3, 10^4	3.7×10^3	$E = 71$ GPa, $\bar{v} = 1.36$ m/s	wave speed
$(T_M - T_R) \cdot c_V/E$	0.005, 0.01, 0.022, 0.05, 0.1	0.022	$T_R = 300$ K, $c_V = 2.48$ MPa/K, $E = 71$ GPa	melt temperature
c_V/c_{V0}	0.1, 0.2, 0.5, 1, 2	1	$c_{V0} = 2.48$ MPa/K	specific heat*
A/E	0.001, 0.003, 0.0042, 0.006, 0.01	0.0042	$E = 71$ GPa	static initial yield
B/A	0, $\frac{1}{3}$, $\frac{2}{3}$, 1, $\frac{5}{3}$	$\frac{2}{3}$	$A = 0.3$ GPa	strain hardening coefficient
n	0, 0.15, 0.3, 0.5, 1	0.3	-	strain hardening exponent
C	0, 0.02, 0.05, 0.1, 0.2	0.05	-	strain rate sensitivity
m	0.5, 1, 1.5, 3, ∞	1	-	thermal softening
$(T_0 - T_R) \cdot c_V/E$	0, 0.0015, 0.0045, 0.0095, 0.0195	0	$T_R = 300$ K, $c_V = 2.48$ MPa/K, $E = 71$ GPa	initial temperature

*For exploration only; E and c_V are normalization factors and not true independent variables in the present dimensional analysis.

System modulus $\bar{E}$ of Eq. 2 quantified in Table 2 accounts for the true elastic modulus of both the indenter and substrate. This value is used in the Hertz solutions ($R_s \rightarrow \infty$) of Section 2.1 that are compared with some forthcoming results. If a rigid indenter is assumed instead, then $\bar{E}$ increases by $\approx$10%. However, since the indenter's material is held fixed among experiments, elastic and other intrinsic properties of the indenter can be excluded from the list of independent variables in the dimensional analysis of Section 4. The initial radius $R = R_i$ of the indenter is also fixed among all experiments and simulations.

3.3 Model Results

Investigated first are effects of FE mesh density on the global indentation response. Meshes of increasing numbers of elements ranging from approximately 387 K to 24.8 M were implemented in simulations with boundary conditions for test 3, which corresponds to the largest indentation force, indentation depth, and local strains among the three tests. Normalized force versus depth is shown in Fig. 4a for four different levels of mesh refinement, along with experimental results and the Hertz elastic solution. The latter is notably stiffer than FE model and experiment at larger depths, since plastic yielding occurs in simulations and experiments. The 387 K element mesh is too coarse, but the 3.1 M element mesh is sufficient to resolve the $P - h$ response, since effects of further increases in numbers of elements are small.

The normalized contact radius from simulations and the Hertz theory is shown in Fig. 4b. The mean contact pressure $p = P/(\pi a^2)$ divided by E of the specimen is shown versus normalized depth in Fig. 4c. Both sets of results show only the loading phase.

The elastic Hertz solution gives a smaller contact radius and larger contact pressure than the elastic-plastic simulations. Although the contact radius appears to be relatively mesh insensitive in Fig. 4b, the contact pressure in Fig. 4c converges rather slowly with increasing number of elements. Oscillations arise when nodes come in and out of contact during the dynamic event. Small changes in a can manifest as large changes in p. Accordingly, when p is of high interest, the more refined 10.5 M element mesh is used subsequently. But when only P vs. h data are studied, the 3.1 M element mesh is used for numerical cost efficiency. Contact oscillations prevented accurate extraction of a or p during the unloading histories.

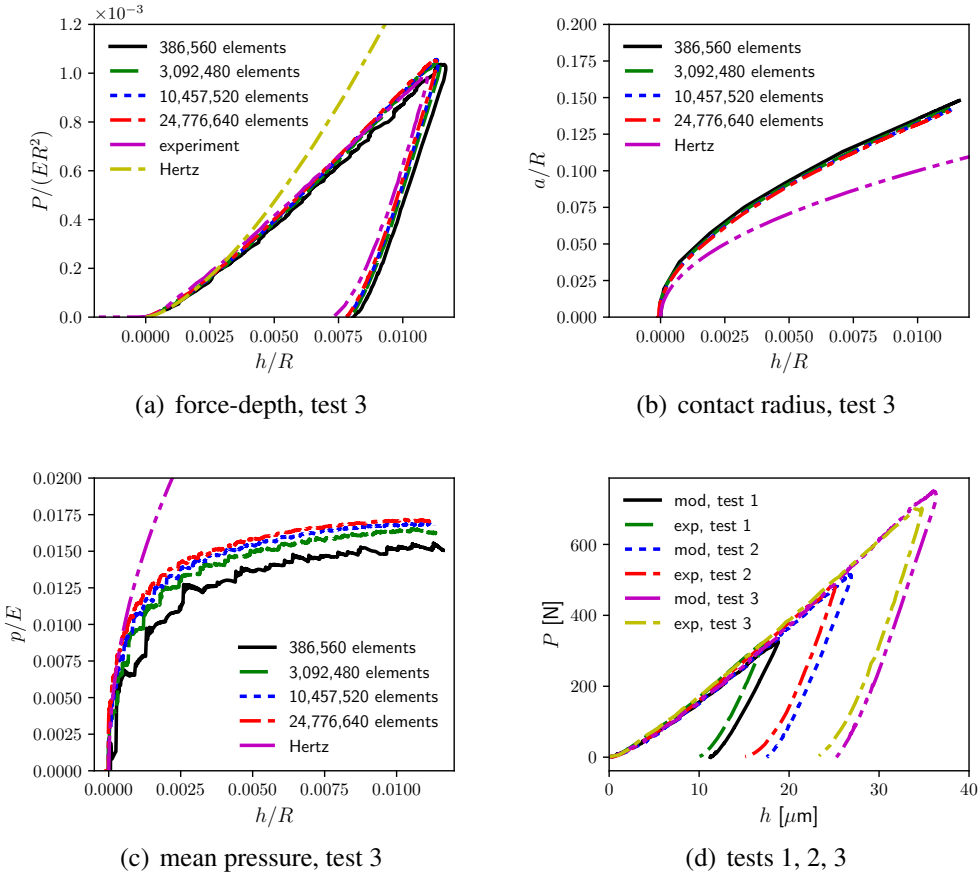

(a) force-depth, test 3

(b) contact radius, test 3

(c) mean pressure, test 3

(d) tests 1, 2, 3

Fig. 4 Baseline simulation results: (a) dimensionless force vs. depth for different mesh densities, test 3 (b) dimensionless contact radius vs. depth for different mesh densities, test 3 (c) dimensionless mean contact pressure vs. depth for different mesh densities, test 3 (d) force vs. depth for all three experiments and simulations (3.1 M element mesh). Contact model is frictionless.

Experimental force-displacement histories are compared with model predictions for all three tests in Fig. 4d. Selected data are also compared in Table 1. For all three tests, the model reasonably reproduces the curvatures of the experimental data for loading and unloading portions. Since the indentation curvatures are primarily dictated by the material properties of the substrate, these similarities suggest that the present constitutive model and parameters (i.e., Johnson-Cook plasticity with parameters of Table 2), are acceptable. However, the maximum load P_m and corresponding peak depth h_m are consistently over-predicted by the simulation, relative to experiment, for all three tests. The discrepancy is thought to arise more from imprecision of representation of the testing geometry and boundary conditions rather than inaccurate constitutive modeling, though the latter cannot be unequivocally

excluded. Uniform scaling of the velocity histories for all three simulations by a factor slightly exceeding unity did not produce improved model agreement for all three tests. Even though "perfect" agreement is not achieved, the present results are deemed sufficiently realistic to warrant further study of local field variables in Section 3. The constitutive parameters are sufficient to serve as "baseline" conditions for parameter sensitivity investigations in the context of dimensional analysis in Section 4.

Similarities and differences between simulations and experiments are quantified for discrete load-unload points in Table 1. Maximum load P_m is over-predicted by 1% to 7%. Corresponding depth h_m is over-predicted by 1.7 to 2.2 μm. Residual depth is over-predicted by 0.8 to 1.6 μm. Simulations also over-predict the residual imprint size a_r; however, identification of the edge of the residual imprint is subjective and imprecise in both model and experiment due to the lip at each edge; tabulated values are considered accurate only to $\pm 10\%$, so errors may be overestimated. Indentation strains (see Section 2.4) based on definitions of $\bar{\epsilon} = 0.2a/R$ of Tabor[61] and $\hat{\epsilon} = 4h/(3\pi a)$ of Pathak and Kalidindi,[2] and their average rates, are listed in the right four columns for simulations in Table 1. Denote by t_m the time duration over which P is increasing, and by a_m the value of contact radius when $P = P_m$ and $h = h_m$. Then the maximum indentation strains and average indentation strain rates listed in Table 1 are computed from, with $R = R_i$ =constant,

$$\bar{\epsilon}_m = 0.2\frac{a_m}{R}, \quad \dot{\bar{\epsilon}} = 0.2\frac{a_m}{R\,t_m}; \qquad \hat{\epsilon}_m = \frac{4}{3\pi}\frac{h_m}{a_m}, \quad \dot{\hat{\epsilon}} = \frac{4}{3\pi}\frac{h_m}{a_m\,t_m}. \tag{21}$$

Peak indentation strains increase from test 1 to test 2 to test 3, as do average indentation strain rates, for both sets of definitions in Eq. 21. This behavior is in qualitative agreement with increasing average applied velocity $\bar{v}$ with increasing test number. Peak indentation strains and average rates are consistently around 20% larger when $\hat{\epsilon}$ rather than $\bar{\epsilon}$ is used for their definitions. With $\hat{\beta} = 1.3$ as an approximation in Eq. 17,[29,53] peak uniaxial equivalent strains range from 2 to 2.5%, and average uniaxial equivalent strain rates from 900 to 1700/s, across the simulations of tests 1, 2, and 3. Experimental values cannot be determined for indentation strains and strain rates since a_m is not measured in the dynamic experiments.

Denote by μ the coefficient of contact friction used for the indenter-specimen interface. Static and dynamic coefficients were assumed equal, and were allowed to vary

among different trial simulations with the input velocity history of test 3. Effects of μ on P, a, and p were found to be negligible on the global $P - h$ response for a reasonable range $\mu \leq 0.2$ (e.g., see other references[54,65,66]) for the moderate velocity input conditions of Fig. 2a, so $\mu = 0$ is used henceforth in Sections 3, 4, and 5. This choice handily eliminates μ from the list of independent variables entering the dimensional analysis of Section 4. The same assumption of frictionless contact was used elsewhere[6] in FE simulations of static spherical indentation with the same Al 6061-T6 substrate and WC indenter materials, wherein close agreement of simulated and experimentally measured[48] data was inferred.

A friction coefficient is difficult to quantify independently for the present experiments, but a frictionless assumption becomes more realistic as the smoothness of surfaces increases. In the current experiments, both the indenter and specimen are polished to a smooth mirror finish. Very small differences in residual indentation profiles, notably the height at the pile-up location (i.e., the lip of the indentation) were detected in dynamic simulations when μ was increased, but the residual contact radius a_r and depth h_r were negligibly different when $\mu = 0.2$ was used. For much higher rates of loading as in the appendix, μ does noticeably affect the load-depth response.

Inconsistent prescriptions of friction coefficients exist among FE studies of indentation in the literature. Differences could be due to different surface conditions of tested materials, but more often values are not rigorously justified. Frictionless contact is assumed in static spherical simulations of Dean and Clyne,[67] while a value of $\mu = 0.15$ is used without apparent explanation in a different study.[66] Frictionless contact appears to be the most common assumption in prior FE simulations of dynamic indentation,[10,11,13,14,21,35] though this assumption is made often for convenience or is not explained. In simulations of dynamic sharp indentation, μ was unstated by Lu et al.,[9] and $\mu = 0.125$ was used elsewhere[65] without apparent explanation. A few more rigorous works have prescribed μ based on calibration of FE models to indentation depth histories and shapes of indentation profiles: a best value of $\mu = 0.1$ was found by Burley et al.[36] while a value of $\mu = 0.2$ was found in other works.[54,68] Also noted from prior ballistic simulations[36] is that frictional effects become more prominent as the indentation rate (i.e., impact velocity) increases. The same conclusion is drawn in the appendix of this work.

Contours of predicted local axial Cauchy stress, local Cauchy pressure, local plastic strain, and local temperature are shown for test 3 at a simulation time of 40 μs in Fig. 5. At this time instant, the load P is $\approx 91\%$ of peak load P_m. Results in Fig. 5a and Fig. 5b show maximum magnitudes of axial stress and pressure around 1.5 and 1.0 GPa, respectively. The maximum plastic strain and temperature rise relative to $T_0 = 300$ K attained in the specimen are approximately 8% and 20 K, respectively, in Fig. 5c and Fig. 5d. According to the Johnson-Cook model and baseline parameters for Al 6061-T6 in Table 2, a 20 K temperature rise would produce a drop in yield strength of only 3.2%. The WC output bar (indenter) shown on the right of each figure does not deform plastically or measurably increase in temperature; maximum local deviatoric stresses remain far below the yield strength of WC.

Surface imprints of the sample are of interest since they may facilitate identification of material properties (if unknown a priori).[65,69] The residual plastic imprint, after complete withdrawal of the indenter, may also be useful for comparison with experimental measurements (Table 1) and estimation of the system modulus $\bar{E}$ during unloading.[49] In Fig. 6a, the increase in imprint size with applied load P is obvious; a substantial amount of elastic recovery between maximum depth at $P = P_m$ and the residual state is also evident. A lip of plastically deformed material is clear in the residual imprint, but it is obscured by elastic deformation during loading. The slope S entering Eq. 5 is estimated from simulation results in Fig. 6b. The value of $S = 78.3$ N/m provides nearly exact confirmation of the system modulus $\bar{E}$ in Table 2 when a_r is used in Eq. 5, as proposed by Oliver and Pharr.[49] If, on the other hand, a_m of Table 1 is used with the same S, Eq. 5 produces a value of $\bar{E}$ around 10% too large. Discrepancies may be due to approximations inherent in the use of Hertz theory, which is here liberally extended to the dynamic elastic-plastic regime.

The basic constitutive model in Eqs. 19 and 20 is viewed as an example of potentially high interest since it is very widely used by the applied engineering community. Other simple constitutive models for rate and temperature sensitivity include power-law forms.[5,9,14,29,70] More elaborate models constructed from physics and materials science arguments exist,[55,71–75] though the relative extent of predictive physics versus phenomenology varies among these. Methods of dimensional analysis set forth in prior work[29] and advanced next in Section 4 should be applicable to other elastic-plastic models if consideration is given to the necessary independent variables (e.g., material parameters entering the constitutive theory).

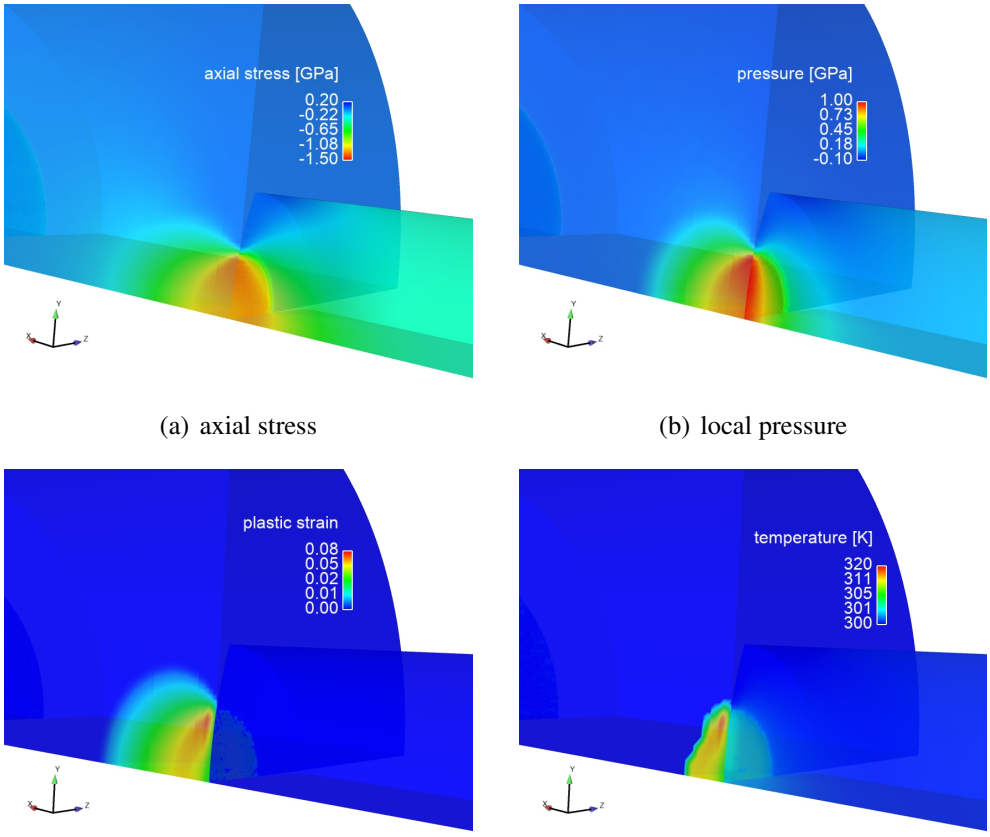

(a) axial stress

(b) local pressure

(c) plastic strain

(d) temperature

Fig. 5 Contours of field variables from simulation of test 3, $t = 40\,\mu$s, $P/P_m = 0.911$: (a) axial Cauchy stress σ_{xx}, (b) local Cauchy pressure $-\frac{1}{3}(\sigma_{xx} + \sigma_{yy} + \sigma_{zz})$, (c) effective plastic strain ϵ^P, and (d) absolute temperature T (3.1 M elements; specimen is on left, indenter and output bar on right)

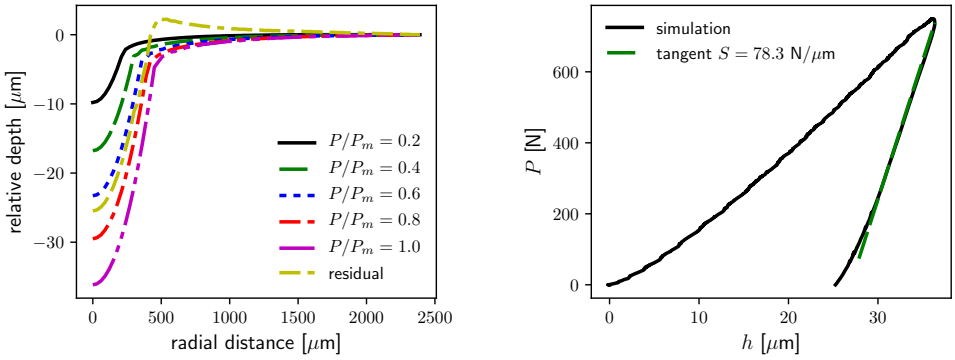

(a) surface imprints, test 3

(b) unloading slope, test 3

Fig. 6 Simulation results for test 3: (a) surface displacement of specimen at load levels P/P_m, where P_m is maximum indentation force and "residual" is final plastic imprint; (b) assessment of slope during unloading for inference/confirmation of system modulus $\bar{E}$

4. Dimensional Analysis and Parameter Sensitivity

Given a sample of solid material with unknown physical properties, a typical objective of indentation experiments is determination of such properties via analysis of load-depth history data, as well as analysis of possibly available information on contact radius and the size and shape of any residual imprint. If functional relationships between the indentation response and constitutive properties are available for a given set of boundary and initial conditions, then it may be possible to invert such relationships to extract constitutive properties. In principle, these functional relationships could be found from experiments alone on a (very large) collection of different materials whose physical properties span the domain of interest. However, if numerical methods are sufficiently accurate, determination of functional relationships between global indentation response and constitutive properties is much more easily and efficiently accomplished using simulations, since many properties can be adjusted in simulations with trivial effort.

Results presented later in Section 4 are directed toward this objective, although no attempt is made to determine invertible analytical relationships, which may not exist. Rather, complexity of the response functions suggests that numerical databases be used,[35] whereby information contained in large databases constructed from numerous FE simulations spanning a sufficiently wide domain of independent dimensionless variables could be compared with experimental findings on new materi-

als to deduce each new material's constitutive properties. Multi-fidelity approaches with surrogate and analytical models[6,44] can be used to reduce computational cost of database population by higher-fidelity FE simulations alone, as appears necessary for the present case of highly refined, explicit 3-D simulations whose results are sensitive to many material properties (Section 4).

Complexity of functional relationships can be mitigated via classical tools of dimensional analysis.[30–32] More specifically, the number of independent variables entering such relationships can be systematically reduced by casting response functions in dimensionless form, then applying Buckingham's Pi theorem to reduce the number of independent quantities by the number of independent physical dimensions entering the problem. This number is four for dynamic indentation, since length, time, mass, and temperature are the physical dimensions of present relevance.

In the analysis that follows, several assumptions are invoked upon consideration of FE simulation results of Section 3. These assumptions reduce the number of possible independent parameters, which simplifies the dimensional analysis. First, with the exception of the indenter radius R, the geometry of dynamic indentation system is assumed fixed, including sizes and shapes of components, and the materials comprising the input bar and indenter/output bar. The length and radius of the cylindrical specimen are fixed, but the substrate material itself can vary; hence, the mass of the specimen varies with its initial density. Therefore, the physical dimensions of the experimental system (except for R) and constitutive properties of the bars can be excluded from the set of independent variables, since these remain fixed. Contact is frictionless, as justified in Section 3.3.

A system velocity, denoted by v, is assumed to be a defined, controllable quantity for each simulation or experiment analyzed, and is not labeled a dependent variable. For example, the system velocity v could be simply assigned as the indenter velocity $\dot{h}$ if constant in a simulation,[13,14,21] or it could be assigned the initial (measured) projectile impact velocity for a spherical impact experiment.[8,76] The indenter velocity in a SHPB experiment is generally not constant, even during the loading phase alone[16,18,19]: a transient period may exist over which the indenter accelerates, and then the indenter always decelerates. The velocity of the striker bar could be used for v as a measure of the input loading rate; otherwise, the average indenter velocity over some finite time interval could be used.[16] The entire input velocity history

$\upsilon(t)$ is the true independent variable associated with the applied loading rate. In the forthcoming analysis, the average input velocity $\bar{\upsilon}$ of Eq. 18 is used for the system velocity for normalization and convenience, since corresponding simulations of Section 4 all impose the same history $\upsilon(t)$. Initial temperature T_0 is assumed to be prescribed uniformly over the sample for any given test.

4.1 Variable Identification

The dimensional analysis considers only global, scalar quantities that are either (1) imposed or extracted from indentation simulations and experiments or (2) homogeneous and stationary material properties. Local field variables are not addressed. Dependent and independent variables in dimensional form are first identified. Dependent variables of interest are defined as follows:

- Indentation force P;
- Indentation contact radius a;
- Mean pressure $p = P/(\pi a^2)$, which is trivially known if P and a are known;
- Indentation strains $\bar{\epsilon}$, $\hat{\epsilon}$ and their rates (e.g., Eqs. 13, 15, and 21);
- Size and shape of the residual imprint if plastic deformation occurs, including residual imprint depth h_r and residual imprint diameter a_r.

Independent variables account for the loading conditions and the constitutive properties of the specimen. The material is assumed to be homogeneous and isotropic elastic-plastic, with linear elasticity sufficient for the elastic response and effects of thermal expansion negligible, as justified in Section 3. The Johnson-Cook constitutive model of Eq. 19 is assumed to be sufficient for representing the inelastic response. Adiabatic conditions are assumed a priori, with $\zeta = 1$ in Eq. 11, as in Section 3, so the only prescribed thermal loading condition is the initial temperature. In dimensional form, independent variables are then elements of the following list of 14 items:

- Indentation depth history $h(t)$;
- Effective indentation (system) velocity history $\upsilon(t)$, producing average input velocity $\bar{\upsilon}$;

- Indenter radius R;
- Initial temperature T_0;
- Substrate initial mass density ρ_0, specific heat per unit volume c_V, and melt temperature T_M;
- Substrate elastic properties E, ν [dropping $(\cdot)_s$ subscripts];
- Substrate plastic properties A, B, C, m, n.

Of these independent variables, h and v vary with time during an indentation simulation or experiment. The first four items listed above dictate the loading conditions. The remaining 10 quantities are material properties. Mass density, melt temperature (at ambient pressure), and specific heat are uniquely defined regardless of constitutive model. Elastic modulus and Poisson's ratio are uniquely defined given that elasticity is isotropic and linear. Plastic properties A, B, C, m, n notably depend on the selection of the Johnson-Cook functional form for yield and flow stress. Moreover, their values may not be unique for a given material, but rather are typically estimated by calibration to traditional stress-strain data across a range of applied strains, strain rates, and initial temperatures. Time is not an explicit independent variable, since given the depth and velocity histories and other independent variables, the time at which a particular depth value h is achieved is determined implicitly[32] (e.g., only two of h, v, t are truly independent). Recall that $\dot{\epsilon}_0$ and T_R entering Eq. 19 are treated as universal constants and thus can be excluded as independent variables.

The number of independent dimensions is four: length, time, mass, and temperature. For the indentation problem,[29,32] it is more convenient to work with stress (recovered from mass, length, and time) than mass, so the four independent dimensions are recast into stress, length, time, and temperature. The following combinations of $E, R, \bar{v}, c_V$ are used as normalization constants:

- Stress: modulus E;
- Length: indenter radius R;
- Time: dynamic loading time scale $\bar{t} = R/\bar{v}$;
- Temperature: normalized inverse specific heat $\bar{T} = E/c_V$.

The elastic modulus is a standard prescription for stress normalization.[28,29,32,33] This is a convenient choice in the context of elastic indentation with a rigid indenter, since then P is directly proportional to E as in Eq. 1 with Eq. 2. Often, h and υ have been used for normalization.[13,14,32] However, in the present simulation framework, it is more convenient to normalize with R and $\bar{\upsilon}$, which are easily held fixed in simulations with the same FE mesh (same indenter geometry) and same velocity history boundary conditions applied across different simulations. In high-throughput experiments, these choices would facilitate use of the same loading apparatus and striker bar velocity while switching out different substrates of the same cylindrical size. Either the melt temperature or specific heat could be used to obtain the normalization temperature. The latter is chosen here since, unlike T_M, it does not explicitly enter the Johnson-Cook Eqs. 19 and 20. As $\bar{T}$ decreases, the tendency for adiabatic temperature rise decreases.

Applying the Pi theorem via normalizing the remaining independent variables, the number of independent variables is reduced from 14 to 10 in dimensionless form when history $\upsilon(t)$ is fixed:

- Indentation depth h/R;
- Poisson's ratio ν;
- Mass density through an elastic wave speed via $C_l\,\bar{t}/R$, where $C_l = \sqrt{E/\rho_0}$;
- Yield strength A/E;
- Strain hardening coefficient B/A;
- Strain hardening exponent n;
- Strain rate sensitivity coefficient C;
- Thermal softening exponent m;
- Initial temperature $(T_0 - T_R)/\bar{T}$;
- Melt temperature $(T_M - T_R)/\bar{T}$.

In the context of this normalization strategy, the Johnson-Cook Eq. 19 for equivalent

yield and flow stress is rewritten in dimensionless form as

$$\frac{1}{E}\sigma(\epsilon^P, \dot{\epsilon}^P, T) = \frac{A}{E}\left[1 + \frac{B}{A}(\epsilon^P)^n\right] \cdot \left[1 + C \cdot \ln\frac{\dot{\epsilon}^P}{\dot{\epsilon}_0}\right] \cdot \left[1 - \left(\frac{\{T - T_R\}/\bar{T}}{\{T_M - T_R\}/\bar{T}}\right)^m\right]. \tag{22}$$

Written in this way, B/A matches the hardening coefficient κ widely used in other generic plasticity models (e.g., Fernandez-Zelaia et al.[6] and Patel and Kalidindi[53]), with $A = \sigma_0$ and n unchanged. As $R/(C_l\,\bar{t}) \to 0$, inertial effects should become less important since stress wave equilibrium should be achieved more rapidly relative to viscoplastic rate effects. As $(T_M - T_R)/\bar{T}$ increases, the thermal softening effect decreases. Ambient temperature T_0 will differ from T_R for preheated samples.

4.2 Functional Forms

Given the independent dimensionless variables, the sought dependent variables can be expressed as dimensionless functions. For example, indentation force and contact radius are Π_P and Π_a:

$$\frac{P}{ER^2} = \Pi_P\left(\frac{h}{R}, \frac{T_0}{\bar{T}}; \frac{T_M}{\bar{T}}, \frac{R/\bar{t}}{\sqrt{E/\rho_0}}, \frac{A}{E}, \frac{B}{A}, C, n, m, \nu\right), \tag{23}$$

$$\frac{a}{R} = \Pi_a\left(\frac{h}{R}, \frac{T_0}{\bar{T}}; \frac{T_M}{\bar{T}}, \frac{R/\bar{t}}{\sqrt{E/\rho_0}}, \frac{A}{E}, \frac{B}{A}, C, n, m, \nu\right). \tag{24}$$

Arguments preceding the semicolons on right sides of Eqs. 23 and 24 are loading conditions, and arguments following the semicolons are material properties. The isothermal, quasi-static Hertz solution of Section 2.1 should be recovered for finite E, R, T_0, T_M as $A/E \to \infty$ (infinite yield strength so behavior remains elastic), $\bar{T} \to 0$ (infinite specific heat so temperature cannot change) with either or both of $\bar{t} \to \infty$ (infinitesimal input velocity) and $C_l \to \infty$ (instantaneous stress propagation), where for $R_s \to \infty$:

$$\Pi_P\left(\frac{h}{R}, \infty; \infty, 0, \infty, \cdot, \cdot, \cdot, \cdot, \nu\right) = \frac{4}{3(1-\nu^2)}\left(\frac{h}{R}\right)^{3/2} \qquad [\bar{R} \to R], \tag{25}$$

$$\Pi_a\left(\frac{h}{R}, \infty; \infty, 0, \infty, \cdot, \cdot, \cdot, \cdot, \nu\right) = \left(\frac{h}{R}\right)^{1/2} \qquad [\bar{R} \to R]. \tag{26}$$

Analytical functional forms, if they exist, should be consistent with elastic limits in Eqs. 25 and 26. Dimensionless functions for the mean contact pressure, constraint

factor relative to $\sigma_0 = A$, and indentation strains can also be constructed from Eqs. 23 and 24:

$$p = \frac{E}{\pi}\left(\frac{R}{a}\right)^2 \cdot \Pi_P \approx c \cdot A, \qquad \bar{\epsilon} = 0.2\frac{a}{R} = 0.2 \cdot \Pi_a, \qquad \hat{\epsilon} = \frac{4}{3\pi}\frac{h}{a} = \frac{4}{3\pi}\frac{h/R}{\Pi_a}. \tag{27}$$

Knowledge of the dimensionless response alone is insufficient for complete property identification through inversion of the response functions for their dimensionless arguments. For example, E is needed to recover A if dimensionless argument A/E is known from $P/(ER^2)$ histories. Fortunately, experimental load-depth data are captured in dimensional form (i.e., P vs. h). Additionally, R, $\bar{t}$, and T_0 are known a priori as prescribed conditions, inserting respective length, time, and temperature dimensions into the true physical problem. If E is not known a priori, its value might be obtained through implicit solution of Eq. 23 given sufficient data on P, where E is to be calibrated along with other constitutive properties. Whether or not this is tractable depends on uniqueness of the response function with respect to the model parameters.

4.3 Parameter Sensitivity Predictions

For a material with unknown physical properties but expected isotropic linear elastic-plastic behavior, a stated goal of instrumented dynamic experiments on samples of such material is determination of its properties for numerical modeling, namely 10 scalar values $(\rho_0, E, \nu, c_V, T_M, A, B, C, m, n)$ in the context of the Johnson-Cook model with linear elasticity and constant specific heat. From the present experimental capabilities, the most abundant data will consist of force-depth curves (P vs. h) obtained from a sample at known initial temperature T_0. Thus, the focus of the current sensitivity study, in the context of dimensional analysis, is understanding effects of independent parameters on the dimensionless force-depth response, that is, Π_P versus h/R, with the functional arguments given by Eq. 23.

The input velocity and its mean, $v(t)$ and $\bar{v}$, could vary among different experiments, as could the radius of the indenter R and the initial temperature T_0. However, only the latter (T_0) is varied among the present simulations. In complementary experiments on each new material, the testing apparatus would be held the same, avoiding the need to change input and output bars and recalibration for a new indenter size. In the FE simulations and dimensional analysis, this avoids the need to generate meshes of new system geometries or redefine the normalization time $\bar{t}$ and

normalization length R. Assuming that Eq. 23 exists, in analytical or more likely numerical (database) form, the objective then would be to determine the 10 scalar material parameters that provide a best fit to experimental P versus h data collected at different T_0 but the same R and $\bar{t}$.

Ranges of parameters studied in subsequent dynamic FE simulations are given in Table 3. Values are chosen to span the domain of properties that may reasonably be expected for engineering metals. Although the baseline values of elastic modulus E and specific heat c_V are used as normalization constants in the dimensional analysis (the latter via $\bar{T} = E/c_V$), effects of these quantities are also explored parametrically. Such exploration is useful since both E and c_V would not be known a priori for a completely uncharacterized material. Test data in dimensional form would need to be used to deduce E and c_V by inversion and implicit fitting of Eq. 23.

Effects of elastic modulus and Poisson's ratio on $\Pi_P = P/(ER^2)$ are shown in Fig. 7 at $T_0 = T_R$. Holding other properties fixed, a halving or doubling of E noticeably softens or stiffens the dimensionless response. Indentation force is relatively less affected by ν, in agreement with other studies.[32,66,77] As ν decreases with E fixed, the bulk modulus decreases, which tends to reduce the indentation stiffness. The rather low sensitivity of the response to ν suggests that P versus h data would not enable extraction of a very precise value.

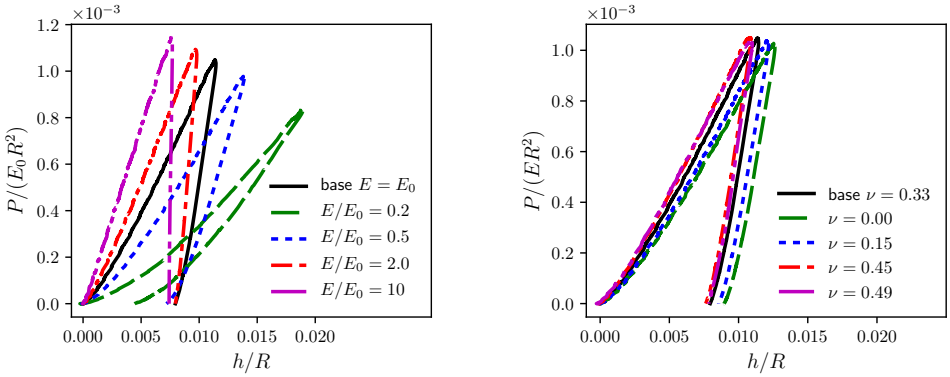

(a) E (b) ν

Fig. 7 Predicted normalized indentation force vs. depth over elastic property ranges of Table 3: (a) dimensionless Young's modulus E/E_0; (b) Poisson's ratio ν. Baseline properties "base" correspond to those of Section 3 and Table 2.

Effects of other thermo-mechanical properties on $\Pi_P = P/(ER^2)$ are shown in

Fig. 8, where here, initial temperature $T_0 = T_R = 300$ K. Elastic wave speed at fixed E has a very small effect on Π_P when varied by a factor of 10 in Fig. 8a. Thus, inertia seems to influence the global force-depth response very little for the present loading conditions. Velocities exceeding 5 m/s may be required to induce noticeable inertial effects on indentation force, as quantified elsewhere for simulations of much higher constant impact velocities.[13] It appears unlikely that instrumented dynamic indentation data collected for the present range of impact velocities would enable much inference about wave speed (i.e., mass density) of an unknown material.

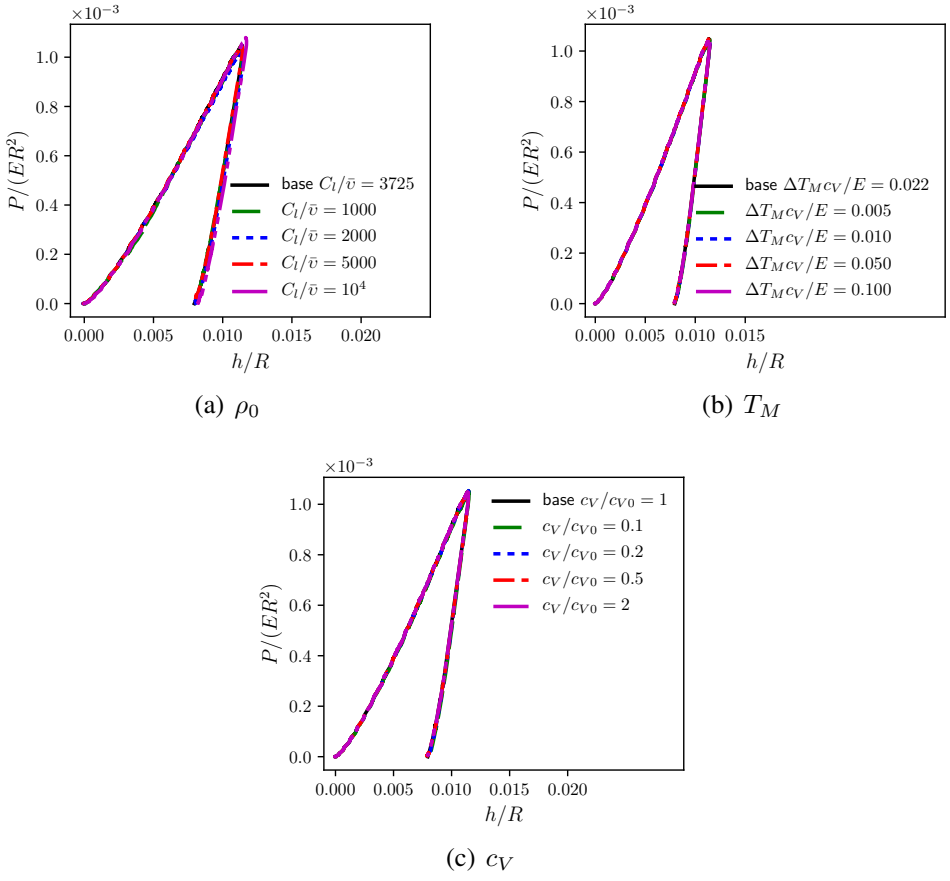

(a) ρ_0 (b) T_M

(c) c_V

Fig. 8 Predicted normalized indentation force vs. depth over thermo-mechanical property ranges of Table 3: (a) dimensionless wave speed $C_l/\bar{v}$ via variation of initial mass density ρ_0, (b) dimensionless melt temperature $(T_M - T_R) \cdot c_V/E$ via variation of T_M, and (c) dimensionless specific heat capacity c_V/c_{V0}. Baseline properties "base" correspond to those of Section 3 and Table 2.

Denoting $\Delta T_M = T_M - T_R$ in Fig. 8b, changing ΔT_M by a factor of 20 negligibly affects Π_P for $T_0 = T_R$. As suggested by findings in Fig. 5d, temperature rise is expected to not exceed 25 K, and is highly localized. Even with T_M reduced

from 925 to 443 K, adiabatic temperature rise is still insufficient to thermally soften the material enough to affect the global force-depth response. As shown in Fig. 8c, increasing or reducing c_V by a factor as much as 10 similarly is insufficient to affect thermal softening for $T_0 = T_R$. The low sensitivity of simulation results to T_M and c_V show that little information regarding the melt temperature or specific heat is afforded by dynamic spherical indentation.

Inelastic constitutive properties are investigated next, specifically those entering the Johnson-Cook framework of Eqs. 19, 20, and 22. Normalized parameters A/E and B/A are considered in respective Figs. 9a and 9b at $T_0 = T_R$. Indentation force Π_P is notably sensitive to variations in both parameters, with stiffness higher when larger values of either parameter are invoked. It appears that information about initial yield stress A and strain hardening coefficient B (at fixed n) could be inferred from measured dynamic P versus h data, though whether unique values of each parameter could be determined from an arbitrary dynamic indentation data set is uncertain.

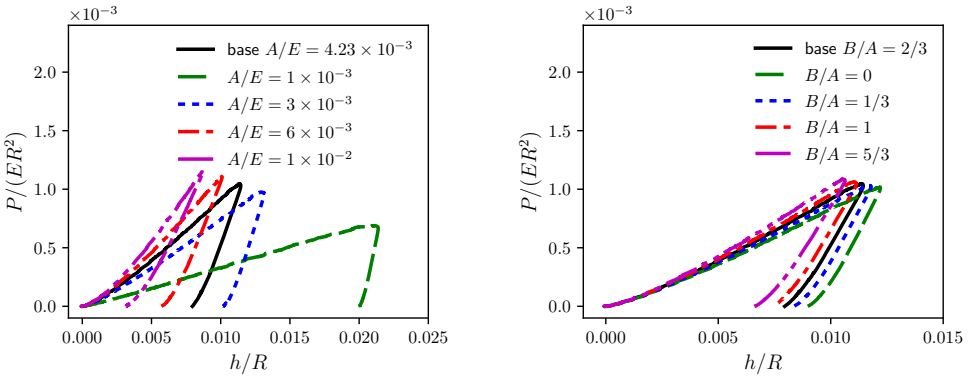

(a) A (b) B

Fig. 9 Predicted normalized indentation force vs. depth over yield and strain hardening coefficient ranges of Table 3: (a) dimensionless initial yield stress A/E via variation of A; (b) dimensionless hardening coefficient B/A via variation of B. Baseline properties "base" correspond to those of Section 3 and Table 2.

Effects of the strain hardening exponent n and strain rate sensitivity factor C are demonstrated in Fig. 10 for $T_0 = T_R$. System stiffness decreases as n increases in Fig. 10a, where the stiffest response arises for $n = 0$, which results in a constant effective static yield strength of $A + B$. Such behavior is not unexpected, since results of Fig. 5c imply that local plastic strain values should remain less than unity

throughout the indentation simulation, so long as departures from baseline properties are not so extreme as to induce plastic strain localization. Sensitivity of results to n is comparable to that of B/A.

Global force-depth response is also notably influenced by strain rate sensitivity parameter C, as evident in Fig. 10b. A straightforward increase in system stiffness is afforded by an increase in C. Changing C by a factor of two significantly affects Π_P in the plastic regime. Similarly to A and B, dynamic indentation data are expected to reveal influences of n and C. Testing at different loading rates could be used to further isolate effects of C.

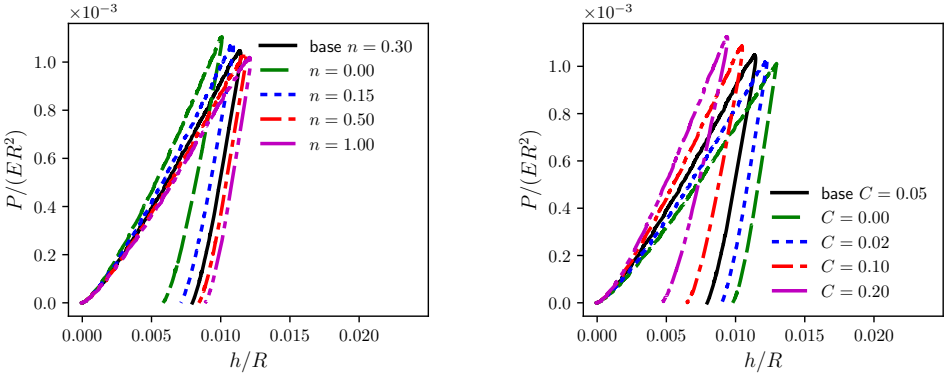

(a) n (b) C

Fig. 10 Predicted normalized indentation force vs. depth over strain hardening exponent and strain rate sensitivity ranges of Table 3: (a) hardening exponent n; (b) rate sensitivity C. Baseline properties "base" correspond to those of Section 3 and Table 2.

Thermal softening parameter m and initial temperature T_0 are studied through FE results of Fig. 11. For $T_0 = T_R$, effects of m on Π_P versus h/R are negligible in Fig. 11a, as expected from contours in Fig. 5d wherein adiabatic temperature rise is localized and small (e.g., not expected to exceed 25 K for baseline parameters). Note that $m \to \infty$ suppresses thermal softening of flow stress in Eq. 19, and reducing m increases thermal softening when other parameters are held fixed.

Effects of increasing the initial specimen temperature T_0 while holding $m = 1$ fixed are shown in Fig. 11b. Thermal softening becomes noticeable for a 50% increase in T_0, to 429 K, and drastic when T_0 approaches T_M (e.g., the softest case shown for 858 K).

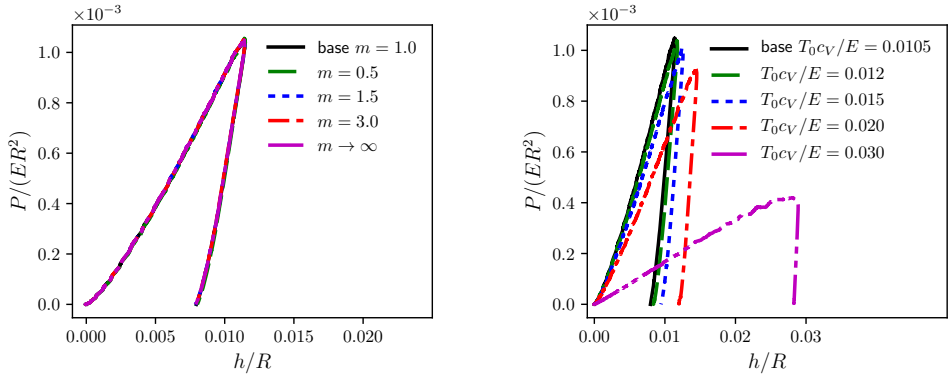

(a) m ($T_0 = 300$ K) (b) T_0 ($m = 1$)

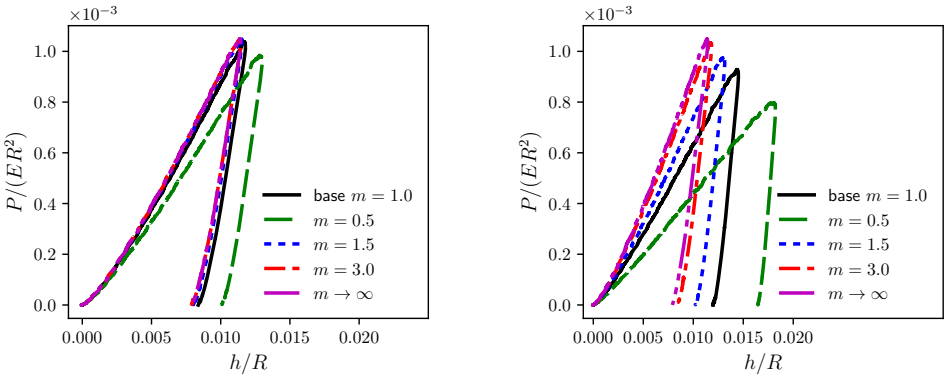

(c) m ($T_0 = 343$ K) (d) m ($T_0 = 572$ K)

Fig. 11 Predicted normalized indentation force vs. depth over thermal softening exponent and initial temperature ranges of Table 3: (a) softening exponent m at $T_0 = T_R$, (b) dimensionless initial temperature $T_0 \cdot c_V/E$ via variation of T_0, (c) softening exponent m at $T_0 = 1.14T_R = 343$ K, and (d) softening exponent m at $T_0 = 1.91T_R$ = 572 K. Baseline properties "base" correspond to those of Section 3 and Table 2.

Effects of m at two elevated initial temperatures (343 and 572 K) are shown respectively in Figs. 11c and 11d. As T_0 increases, Π_P becomes more sensitive to variations in m. Collectively, the present results imply that room-temperature data from instrumented dynamic spherical indentation at the present moderate rates would not be useful for determination of m. Thermal softening is more prominent at higher loading rates of the appendix and other works on ballistic spherical impact.[11,36] Results imply that data collected at higher initial specimen temperatures and the current moderate loading rates could likely facilitate its quantification.

Among the independent constitutive parameters investigated in the current study, all except two would be expected to affect the quasi-static indentation response at room temperature and/or elevated temperatures. The two properties unique to dynamic indentation are the mass density (manifesting via the wave speed C_l) and the plastic strain rate sensitivity (manifesting in the Johnson-Cook model via C). As shown in Fig. 8a, inertial effects appear to be nearly insignificant for the present conditions, so C_l does not warrant closer investigation.

However, C significantly affects results for Π_P in Fig. 10b. To supplement the Π_P versus h/R information, considered next are simulation results on contact radius, mean contact pressure, and indentation strain for different choices of C. Although such history data are not presently available from the dynamic indentation experiments of Section 3, examination of corresponding history data from simulations provides insight into how useful such data could be were it to become available in the future, if and when the contact radius a could be measured in the dynamic experiments.

Shown in Fig. 12 are $\Pi_a = a/R$ of Eq. 24 and p/E, the latter represented versus indentation depth as well as versus the indentation strain $\hat{\epsilon}$ of Pathak and Kalidindi[2] as listed in the last part of Eq. 27. Results correspond to T_0 of room temperature. As evident in Fig. 12a, contact radius decreases with increasing C. Since force P simultaneously increases with C as in Fig. 10b, the contact pressure $p = P/(\pi a^2)$ significantly increases with strain rate sensitivity, more so than P itself. This suggests that contact pressure should be a better result from which to calibrate C than total contact force, since influences of C are magnified.

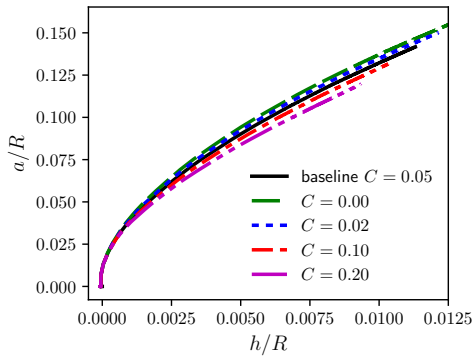

(a) contact radius vs. depth

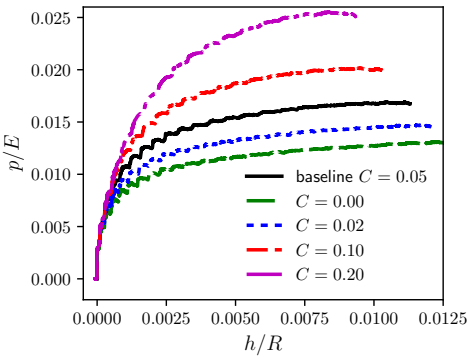

(b) contact pressure vs. depth

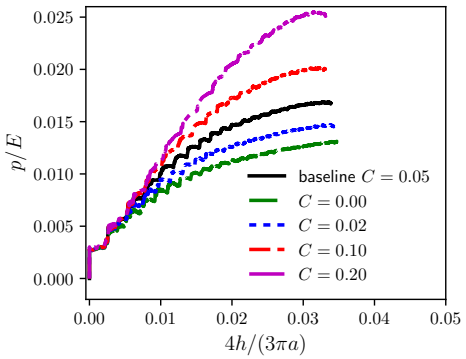

(c) contact pressure vs. indentation strain

Fig. 12 Predicted response functions for variations of strain rate sensitivity parameter C over ranges in Table 3: (a) dimensionless contact radius a/R, (b) dimensionless pressure p/E vs. normalized depth h/R, and (c) dimensionless pressure p/E vs. indentation strain $\hat{\epsilon} = 4h/(3\pi a)$. Baseline $C = 0.05$ corresponds to Section 3 and Table 2; refined 10.5 M element mesh used to better resolve pressure and indentation strain.

Results of p/E versus normalized indentation depth and indentation strain (i.e., indentation stress-strain curves) provide similar visual insight in respective Fig. 12b and Fig. 12c. The transient constraint factor c is obtained by multiplying p/E by $E/A = 236.7$. At maximum load, c ranges from 3.10 for $C = 0$, similar to what would be expected for a mildly hardening, rate insensitive material,[50,61] to a much larger value of 5.94 for $C = 0.2$ wherein plastic strength is drastically increased by rate sensitivity.

Another opportunity for constitutive property extraction arises from examination of surface imprints, for example calibration of constitutive parameters to provide closest agreement between simulated and measured profiles. Simulations provide indentation surface profiles throughout the deformation history. Focusing again on rate sensitivity parameter C of unique interest to dynamic indentation, predicted surface profiles are shown for four values of C in Fig. 13, all at $T_0 = T_R$. For completeness, the baseline case is shown already in Fig. 6a. Imprints are notably affected by C. As C increases, the maximum residual imprint depth decreases, as does the sharpness of the lip along the edge of the crater. Such findings confirm that surface imprints provide useful supplementary information for determination of strain rate sensitivity from instrumented dynamic spherical indentation. This agrees with prior studies of ballistic spherical impact.[11,36]

Presently, experiments provide coarse size estimates of residual imprints via inspection of images from a confocal microscope. Displacement profilometry may be pursued in the future, to acquire accurate profile shapes from recovered specimens and enable refinement or confirmation of model parameters and friction coefficients.[36,68]

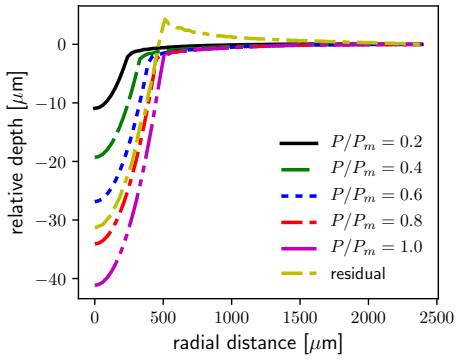

(a) surface profiles, $C = 0$

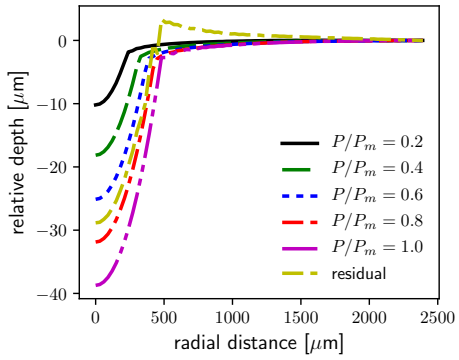

(b) surface profiles, $C = 0.02$

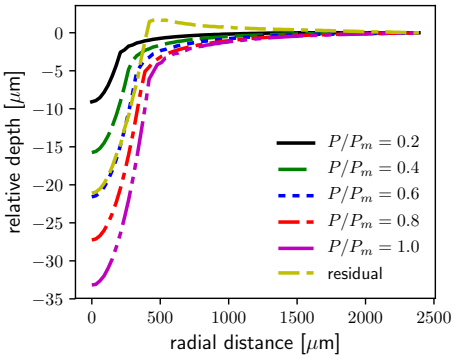

(c) surface profiles, $C = 0.1$

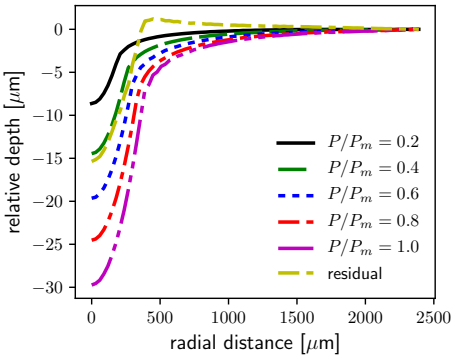

(d) surface profiles, $C = 0.2$

Fig. 13 Surface displacement of specimen at load levels P/P_m, where P_m is maximum indentation force and "residual" is final plastic imprint variations of strain rate sensitivity parameter C over ranges in Table 3: (a) $C = 0$, (b) $C = 0.02$, (c) $C = 0.1$, and (d) $C = 0.2$. Baseline result for $C = 0.05$ is shown in Fig. 6a of Section 3.

4.4 Simulated Strain Rates

Effective strain rates witnessed in the present simulations can be calculated in several ways. First, using results on peak depth, contact radius, and time over which load increases, the indentation strain rates from Eq. 21 as quantified in Table 1 are obtained for all three tests. Values range from 1100/s to 2600/s depending on test number and indentation strain definition. Strain rates based on Tabor's definition $\bar{\epsilon}$[61] are around 20% smaller than those based on Pathak and Kalidindi's $\hat{\epsilon}$.[2]

Second, an average plastic strain rate can be estimated by dividing the plastic strain in the indented zone by the simulation time. For test 3, $\epsilon^P \approx 0.1$ was achieved locally over a load time of 50 μs, giving $\dot{\epsilon}^P \approx 2000$/s, which agrees within 25% of the indentation strain rates in Table 1.

Third, an effective plastic strain rate can be deduced by comparing the increase in indentation stress p observed in Fig. 12(c) between simulations with $C = 0.05$ (which reasonably matches experimental P vs. h data, to be slightly refined to $C = 0.055$ for test 3 in Section 5) and $C = 0$, which replicates static conditions since inertial and thermal effects are small. According to analysis of static indentation,[2,48,61] $p = c\bar{\sigma}$, where $\bar{\sigma}$ is the uniaxial flow stress and c is a constraint factor ranging from 2 to 3. Assuming the same proportionality factor c applies in the moderately dynamic regime, the effective plastic strain rate is obtained by inversion of the Johnson-Cook relation Eq. 19 with $\sigma = \bar{\sigma}$ and $\dot{\epsilon}_0 = 1$/s as $\dot{\epsilon}^P \approx \exp[(p_{|C=0.05}/p_{|C=0} - 1)/C] \approx 800$ m/s: for deep indentation with $h/R \gtrsim 0.01$, mean stress p for $C = 0.05$ is $\approx \frac{4}{3}$ that for $C = 0$ (i.e., dynamic stress is 33% higher than static). This 800 m/s estimate is $\approx \frac{1}{3}$ to $\frac{1}{2}$ those of the other two strain rate estimates.

4.5 Summary and Recommendations

Conclusions from the sensitivity analysis are collected in Table 4. Those constitutive properties that significantly affect the global indentation response data (i.e., Π_P) are candidates for extraction from instrumented dynamic spherical indentation. Those that do not should be determined using other methods such as those proposed in the rightmost column of Table 4. Specifically, pragmatic traditional alternatives[78–80] to indentation are recommended to determine mass density ρ_0, melt temperature T_M, and specific heat per unit volume at constant volume c_V. Precision of dynamic indentation experiments in the very small-depth regime is likely insufficient to directly ascertain elastic compliance via comparison with Hertz's solution.

Table 4 Effects of constitutive parameters on dynamic force-depth response (Y:= very significant) at room and elevated temperatures for dynamic indentation strain rates on the order of 10^3/s, and recommended experiments for their determination. At rates $\gtrsim 10^4$/s, effects of inertial and thermal properties become significant for $T_0 \approx T_R$, and contact friction becomes increasingly important.

Constitutive parameter	Affects $P-h$ $T_0 \approx T_R$	Affects $P-h$ $T_0 \gg T_R$	Suggested experiment
E	Y	Y	wave speed
ν	Y	Y	wave speed
ρ_0	N	N	Archimedes
c_V	N	N	calorimetry
T_M	N	Y	traditional melt
A	Y	Y	static indentation or traditional tension*
B	Y	Y	static indentation or traditional tension*
n	Y	Y	static indentation or traditional tension*
m	N	Y	high-T indentation or high-T tension*
C	Y	Y	dynamic indentation (rates $\approx 10^3$/s)
			traditional Kolsky bar (rates $\lesssim 10^4$/s)
			mini SHPB,[22] ballistic or plate impact ($\gtrsim 10^5$/s)

*Traditional (e.g., Instron machine) compression or torsion also admissible

Thus, wave speed measurements (i.e., conventional ultrasound[81]) are suggested as pragmatic alternatives to accurately measure E and ν, once ρ_0 is found.

It is emphasized that conclusions drawn from the current sensitivity study are limited to moderate strain rates achieved by input velocities on the order of 1 m/s, leading to average indentation depth rates ranging from 1 to 3 m/s and average strain rates on the order of 10^3/s (Table 1 and Section 4.4). As shown by dynamic simulations in the appendix and in other works,[11,14,36] increasing the loading rate by a factor of 10+ leads to increasingly prominent roles of thermal sensitivity, mass density and nonlinear compressibility (affecting shock waves), and contact friction. Much higher effective strain rates can be achieved in ballistic impact, ranging from 10^4 to 10^6/s. Thus, a value of C extracted from higher velocity tests would be more accurate for strain rates in the ballistic range, whereas the presently determined value of C is applicable to moderate strain rates of $\approx 10^3$/s. As noted in Section 5, Al 6061-T6 and some other metals show an increase in strain-rate hardening at rates $\gtrsim 10^4$/s, likely due to increased dislocation drag.[41,72] The Johnson-Cook (one-parameter) rate sensitivity model of Eq. 19 is unable to account for this transition; a more sophisticated model[72] may be more realistic for addressing the full range of rates up to the shock and ballistic regime.

Even though five Johnson-Cook parameters A, B, C, m, n and elastic properties

E, ν affect the dynamic indentation response when different initial temperatures are considered, whether or not reasonably unique values of all parameters could be extracted from instrumented dynamic spherical indentation data at a single representative loading rate is unknown, since multiple constitutive parameters may affect the P versus h response similarly. Some non-uniqueness is inherent in the Johnson-Cook parameters even when calibrated to traditional stress-strain data, as evidenced by property ranges reported elsewhere for Al 6061-T6, for example.[22,40–42,64]

A potentially more robust strategy, avoiding traditional uniaxial stress-strain testing, would obtain rate insensitive properties A, B, and n from static indentation data using previously documented procedures,[6,67] then strain rate sensitivity parameter C from dynamic indentation on a specimen initially at room temperature, and finally temperature sensitivity parameter m from indentation on a specimen at sufficiently elevated initial temperature. In Section 5, this strategy is used to acquire a value of C that produces best fits of work of dynamic indentation from simulations to the present experimental data. The experimental setup is being augmented to permit elevated temperature testing (e.g., for extraction of m); when established and operational, details will be reported in future work.

As shown in Section 5, given static properties A, B, n (independently validated herein vs. static indentation data[48]), the dynamic indentation strain rates achieved in the present study are sufficient to enable determination of a reasonable value of C that falls within bounds of other investigations.[41,42] However, modest differences in input pulse magnitudes and shapes among the 3 tests in Fig. 2(a) produce very similar $P - h$ response curves up to maximum loads, which differ depending on the average magnitude of input velocity. Such similarities persist for simulations in the appendix for input velocities varying by factors of $\frac{1}{2}$ to 2. If static *and* dynamic properties A, B, n, and C were needed to be extracted *solely* from dynamic indentation data, then the present dynamic indentation experiments wound need to be redesigned to accommodate a much wider range of velocities.

Reducing R could enable a higher strain rate, but as explained in Section 3.1, shrinking the dimensions of the system by only a factor of $\frac{1}{2}$—approximately increasing the strain rate by a factor of 2 at fixed P and load duration—would produce an indented volume at yield that contains too few grains to be considered homogeneous and isotropic. As shown in the appendix, a simulated increase in loading rate by

only a factor of two shows very little difference in response other than increased depth (as expected given $C \ll 1$), so decreasing R by $\frac{1}{2}$ would appear to produce little additional useful information. Lowering the input velocity could reduce the strain rate accordingly, but reduction by a factor of $\frac{1}{2}$ produces too little plastic deformation for the same pulse duration, where the latter is limited by the length and wave speed of the striker bar.

Also as shown in the appendix, increasing the indentation rate by a factor between 2 and 5 leads to penetration of the specimen by the cylindrical edge of the output bar, which invalidates analysis of the response as one of spherical indentation. Rather, the problem becomes one of long-rod ballistic penetration. Increasing the rate by a factor between 5 and 10 produces stresses large enough to damage (i.e., plastically deform) other system components such as the input bar and striker interface. In order to achieve higher striking velocities without damaging the system, its physical dimensions could be increased, but this requires a significant rebuild of the device. This proposition is not pursued further since strain rates obtained elsewhere in full-sized instrumented experiments enabling sharp indenters with impact speeds up to 50 m/s[9] produced strain rates on the order of 10^3/s, which are no greater than those achieved here with a miniaturized system. Furthermore, the dimensional analysis of Section 4 assumes that the geometry of the system is fixed except for the indenter radius R.

Pulse shapers could be used to alter the input velocity history profiles, but this proposition also appears unpromising given the similarity of responses for different shaped pulses observed in the existing data. Some variations in aspect ratios and construction materials of the input, output, and striker bars could be accommodated, but their dimensions are restricted by pragmatic constraints[22] including the requirement that stress waves in the bars be 1-D (i.e., rods rather than plates).

Thus, the present work suggests that the instrumented dynamic indentation technique used here is restricted to strain rates on the order of 10^3/s. Much lower spherical indentation rates should be studied using quasi-static or mildly dynamic (velocity-controlled) methods,[2,35] and much higher spherical indentation rates should be studied using ballistic impact.[11,36] These limitations and recommendations are highlighted in Table 4. Other listed techniques could be used to achieve very high loading rates (e.g., normal or inclined plate impact, laser shock), but extraction of

dynamic plastic properties from shockwave data is complicated.[55]

Benefits of the miniaturized indentation system over macroscale systems include its small size and portability (the present system fits on a tabletop, whereas a standard Kolsky bar or plate impact device occupies an entire laboratory room), and its requirement of relatively small samples of material. Once perfected, the miniaturized system should enable low-cost, high-throughput testing of many small samples of differently fabricated materials in a relatively short time, albeit limited to the moderately dynamic rate regime.

5. Johnson-Cook Parameter Determination

An ultimate goal of the combined experimental-numerical approach is identification of elastic, plastic, and other constitutive properties of the indented material. Results in Section 4 show that at modest input velocities (order of one to several m/s) and initial room temperature (not elevated temperature) conditions, the load depth (P vs. h) response is sensitive to elastic constants E, ν and the Johnson-Cook yield and hardening parameters A, B, C, n. A brute-force calibration of all six elastic and plastic parameters, with 10 levels per parameter, would thus require 10^6 simulations to arrive at a best fit for a single experiment. Even if E and ν are assumed known a priori (e.g., via ultrasonic determination), 10^4 simulations would be required per experiment. This number exceeds computational resources with higher-fidelity models alone, considering the expense of dynamic 3-D simulations with over 3 M hexahedral elements needed to model the experimental setup with sufficient mesh resolution. Advanced multi-fidelity approaches (e.g., surrogate and analytical models[6,44]), outside the present scope, can be pursued in the future to alleviate computational burden.

Therefore, guided by the findings of the sensitivity analysis of Section 4, the present study seeks to extract a best value for the dynamic rate sensitivity parameter C, assuming that the elastic (E, ν) and quasi-static properties (A, B, n) are known a priori from external testing. A similar strategy was used for property extraction from ballistic spherical impact, limited to Johnson-Cook parameter C and friction coefficient μ by Burley et al.[36] or C alone by Ito and Arai.[11] Also, using FE simulations of standard Kolsky bar tests, only C and thermal sensitivity m were extracted in prior works[37,38] with the understanding that A, B, n could be easily obtained by a priori fitting of the Johnson-Cook equation to quasi-static data. The same assumptions

are invoked here, noting that static indentation experiments and FE models have been well developed elsewhere[6,67] to obtain yield and power-law strain hardening properties such as A, B and n.

Determination of C is achieved by varying its value over the physically anticipated domain $C \in [0, 0.1]$, in increments of 0.005. Simulation results are compared with experimental data for tests 2 and 3, noting from Fig. 4 that the loading in test 1 (shallow final indentation depth) is largely elastic, so plastic properties cannot be as well identified. Only $P - h$ data from the loading phase of each test, up to peak depths around h_m, are compared in the calibration procedure, since unloading is dominated by elastic rather than plastic properties.

The metric used to determine a best value of C is minimization of the error defined in Eq. 28 as the normalized, cumulative absolute value of the difference between experimental $(\cdot)_{\text{exp}}$ and simulated $(\cdot)_{\text{sim}}$ indentation force P:

$$\begin{aligned} \text{normalized error} &= \left[(1/W_{\text{exp}}) \int_0^{h_m} |P_{\text{sim}}(h) - P_{\text{exp}}(h)| \mathrm{d}h \right], \\ W_{\text{exp}} &= \int_0^{h_m} P_{\text{exp}}(h) \mathrm{d}h. \end{aligned} \tag{28}$$

This error essentially measures the magnitude of the difference in areas under load-depth curves between experiments and simulations, that is, the normalized difference in work of indentation W. Error is calculated for each test and for both in combination, where the latter uses the summed cumulative differences in the numerator and the sum of both experimental W in the denominator of Eq. 28_1.

Force-depth curves for $C \in [0.45, 0.65]$ are shown in Figs. 14a and 14b for respective tests 2 and 3. Normalized errors for each test and totaled are shown in Fig. 14c. A best fit of $C = 0.065$ is obtained for test 2 with an error measure of 1.5% and a best fit of $C = 0.55$ for test 3 with an error of 3.0%. The optimum value for both tests is $C = 0.060$, with a normalized error of 2.8%. This calibrated value of C refines the initial guess of $C = 0.05$ that was used for baseline and parameter studies in Sections 3 and 4. Recall that the initial guess on C, along with assumed values of A, B, n, m, and T_R, were not calibrated to indentation results, but rather were chosen as order-of-magnitude estimates within ranges available from other sources on Al 6061.[22,40–42,64]

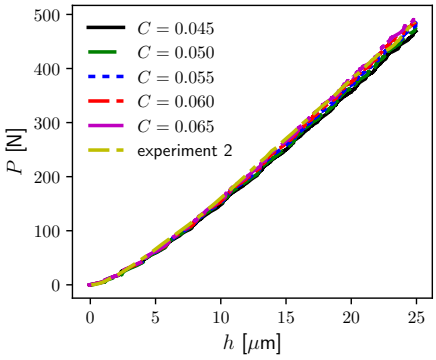

(a) force-depth, test 2

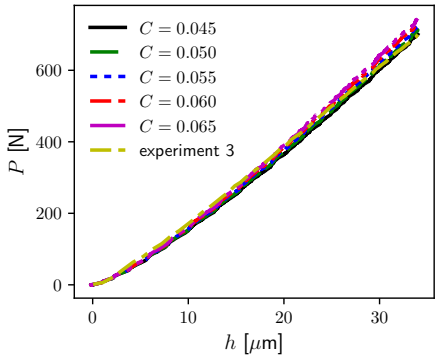

(b) force-depth, test 3

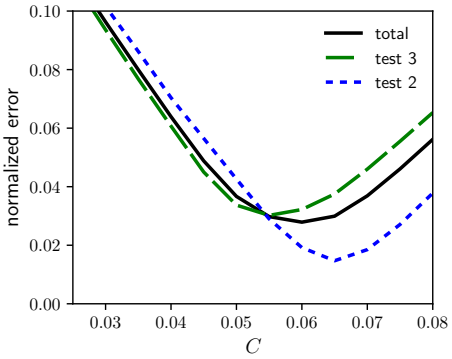

(c) error in predicted work of indentation

Fig. 14 On extraction of Johnson-Cook rate parameter C from dynamic indentation experiments and simulations: (a) indentation force P vs. depth h for loading phase of test 2, range of C in simulations, (b) indentation force P vs. depth h for loading phase of test 3, range of C in simulations, and (c) error in work of indentation W for each test and total (minimized at $C = 0.06$)

Johnson-Cook parameters used in the current work for indentation are compared with those obtained from other experimental investigations in Table 5. The reference by Zhu et al.[42] contains two parameter sets: one for specimen sizes of 25 mm, the other for 50-mm specimens. Corresponding predictions of the flow stress under 1-D plastic strain (uniaxial stress conditions) from the Johnson-Cook equation Eq. 19 are compared in Fig. 15 using these four tabulated sets of parameters, for strain rates ranging from quasi-static (10^{-3}/s) to dynamic (10^{3}/s).

Table 5 Johnson-Cook parameters of Al 6061-T6 from present study and other experiments

Source	Loading	A [GPa]	B [GPa]	n	C	T_R	m
Present work	dynamic indentation	0.300	0.200	0.300	0.060	300	1.00
Zhu et al. (1)[42]	static and dynamic tension (25 mm)	0.203	0.244	0.427	0.083	-	-
Zhu et al. (2)[42]	static and dynamic tension (50 mm)	0.236	0.430	0.376	0.024	-	-
Lesuer et al.[41]	static testing and macro Kolsky bar	0.324	0.114	0.420	0.002	294	1.34

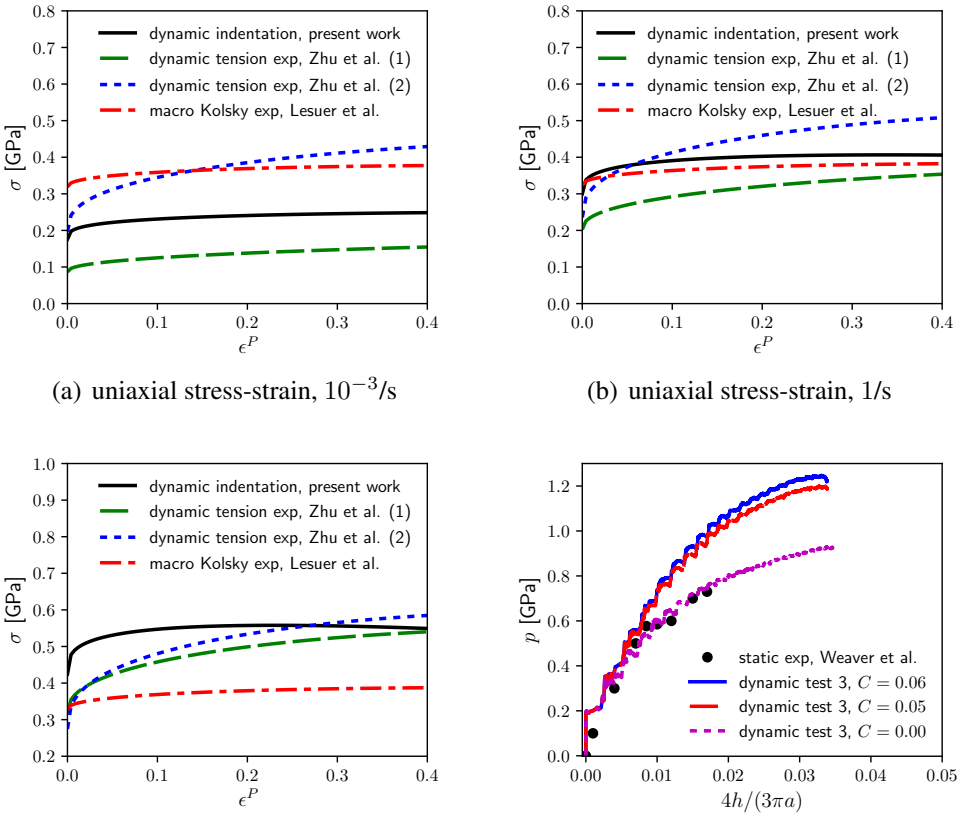

(a) uniaxial stress-strain, 10^{-3}/s

(b) uniaxial stress-strain, 1/s

(c) uniaxial stress-strain, 10^3/s

(d) indentation stress-strain

Fig. 15 Comparison of Johnson-Cook model results with parameters from indentation (present work) and other experiments[41,42] (a) flow stress σ vs. plastic strain ϵ^P for strain rate $\dot{\epsilon}^P = 10^{-3}$/s, (b) flow stress σ vs. plastic strain ϵ^P for strain rate $\dot{\epsilon}^P = 1$/s, (c) flow stress σ vs. plastic strain ϵ^P for strain rate $\dot{\epsilon}^P = 10^3$/s, and (d) indentation stress (mean pressure) $p = P/(\pi a^2)$ vs. indentation strain $\hat{\epsilon} = 4h/(3\pi a)$ from indentation simulations and static indentation data[48]

Most of the current curves fall in between those of other external studies. All athermal parameters except n, which is slightly lower, are within bounds set by the other three external parameter sets. However, not shown in Table 5, the library parameters[40] for Al 6061 encompass values of $n \leq 0.259$, $m \leq 1.0$, $C \geq 0.1$, and $T_R \geq 300$ K. So the present parameter set lies within previously established experimental bounds.

As measured by Nicholas and Lesuer et al.,[41,64] the Al 6061-T6 alloy demonstrates enhanced hardening at strain rates exceeding 10^3/s that cannot be adequately fit using the Johnson-Cook model with one value of C. This transition is attributed to a change from obstacle-controlled to drag-controlled dislocation glide resistance. Similar phenomena have been noted for other metals.[72] The higher hardening rate at low strain demonstrated by the parameters of this study at $\dot{\epsilon}^P = 10^3$/s in Fig. 15c may reflect this or other mechanisms appearing more prominently in dynamic indentation than at milder dynamic rates of focus in other works.[42,64]

Another independent validation of the present set of Johnson-Cook parameters is observed by comparing indentation stress-strain curves[2] from the current simulations with experimental static indentation stress-strain data obtained elsewhere[48] on the same as-received Al 6061-T6 material, with WC likewise used for the spherical indenter. The present simulations with $C = 0$ replicate quasi-static loading, since results in Section 4 confirm that inertia and temperature rise have an insignificant effect on P at the moderate loading rate (mean indenter speed < 3 m/s) of test 3. Close agreement of the simulation with $C = 0$ and the static experimental data confirm that the choices of A, B, and n in Table 5 are valid for indentation studies. The 30%+ increase in mean stress p (deep indentation) for the dynamic cases with $C \in [0.05, 0.06]$ relative to static cases verifies that rate sensitivity is easily discerned by comparing static indentation with the present dynamic indentation method.

6. Conclusions

Simulations of instrumented dynamic indentation experiments in a miniature Kolsky bar have been performed. The tested material is aluminum alloy Al 6061-T6. The FE model, with representative baseline material parameters obtained from the literature for Johnson-Cook plasticity, reasonably replicates the curvature of the experimental load versus depth data for three different experimental loading histories corresponding to different velocity profiles for the Kolsky input bar. Uniaxial-equivalent strain rates for simulations of these three experiments, averaged over their time histories, have been estimated from indentation strain rates to range from 900 to 1700/s. For baseline properties, maximum local plastic strains have been calculated on the order of 10%, leading to maximum local adiabatic temperature rise on the order of 25 K. This rise has been found to be insufficient to significantly affect load-depth curves through thermal softening at these moderate dynamic rates.

A framework for dimensional analysis of instrumented dynamic spherical indentation has been implemented. Parametric FE simulations have revealed the sensitivity, or lack thereof, of the predicted response to variations in the independent variables encompassing material properties and loading protocols. The sensitivity analysis has shown that the global indentation force versus indentation depth response for dynamic loading is significantly influenced by four Johnson-Cook plasticity parameters for specimens initially at room temperature: the initial yield strength A, the strain hardening coefficient B, the strain hardening exponent n, and the strain rate sensitivity factor C. For specimens at initially high temperatures, the global response is also significantly influenced by the thermal softening parameter m.

A combination of room- and elevated-temperature tests is recommended for extraction of Johnson-Cook parameters for previously uncharacterized ductile materials, where static indentation is recommended to inform A, B, and n and dynamic indentation is recommended to inform C. The present experimental setup is realistically restricted to effective strain rates on the order of 10^3/s. Experimental methods other than dynamic instrumented indentation are recommended for determination of mass density, melting temperature, specific heat, and linear elastic constants, since these parameters either too weakly affect the global response or cannot be obtained pragmatically at high precision, given the fidelity of available dynamic indentation data.

Extraction of C from the present dynamic data and simulations has been demon-

strated and reasonably validated, with a few exceptions, versus independent experimental sources for strain rates up to the order of 10^3/s. For confirmation of C pertinent to much higher loading rates, other techniques such as ballistic impact should be considered. Inertial, thermal, and frictional properties become increasingly important in the ballistic regime.

7. References

1. Kalidindi S, Pathak S. Determination of the effective zero-point and the extraction of spherical nanoindentation stress–strain curves. Acta Materialia. 2008;56:3523–3532.

2. Pathak S, Kalidindi S. Spherical nanoindentation stress–strain curves. Materials Science and Engineering R. 2015;91:1–36.

3. Taljat B, Zacharia T, Kosel F. New analytical procedure to determine stress-strain curve from spherical indentation data. International Journal of Solids and Structures. 1998;35:4411–4426.

4. Mesarovic S, Fleck N. Spherical indentation of elastic–plastic solids. Proceedings of the Royal Society of London A. 1999;455:2707–2728.

5. Clayton J. Spherical indentation in elastoplastic materials: modeling and simulation. US Army Research Laboratory; 2005. Report No.: ARL-TR-3516.

6. Fernandez-Zelaia P, Joseph V, Kalidindi S, Melkote S. Estimating mechanical properties from spherical indentation using bayesian approaches. Materials & Design. 2018;147:92–105.

7. Johnson K. Contact mechanics. Cambridge University Press; 1985.

8. Mok CH, Duffy J. The dynamic stress-strain relation of metals as determined from impact tests with a hard ball. International Journal of Mechanical Sciences. 1965;7:355–371.

9. Lu J, Suresh S, Ravichandran G. Dynamic indentation for determining the strain rate sensitivity of metals. Journal of the Mechanics and Physics of Solids. 2003;51:1923–1938.

10. Calle M, Mazzariol L, Alves M. Strain rate sensitivity assessment of metallic materials by mechanical indentation tests. Materials Science and Engineering A. 2018;725:274–282.

11. Ito K, Arai M. Simple estimation method for strain rate sensitivity based on the difference between the indentation sizes formed by spherical-shaped impactors. International Journal of Mechanical Sciences. 2021;189:106007.

12. Kren A, Rudnitskii V, Lantsman G, Khudoley A. Influence of the dynamic indentation parameters on the behavior of metals during the penetration of an indenter with a spherical tip. Russian Metallurgy. 2021;2021:563–569.

13. Lee A, Komvopoulos K. Dynamic spherical indentation of elastic-plastic solids. International Journal of Solids and Structures. 2018;146:180–191.

14. Lee A, Komvopoulos K. Dynamic spherical indentation of strain hardening materials with and without strain rate dependent deformation behavior. Mechanics of Materials. 2019;133:128–137.

15. Anton R, Subhash G. Dynamic Vickers indentation of brittle materials. Wear. 2000;239:27–35.

16. Subhash G. Dynamic indentation testing. ASM Handbook on Mechanical Testing and Evaluation. 2000;8:519–529.

17. Li S, Haozhe L. A new technique of dynamic spherical indentation based on SHPB. In: Dynamic Behavior of Materials; Vol. 1. Song B, Casem D, Kimberley J, editors. Springer; 2014. p. 81–87.

18. Casem D, Pittari J, Swab J. High-rate indentation using miniature Kolsky bar methods. In: Dynamic Behavior of Materials; Vol. 1. Mates S, Eliasson V, editors. Springer; 2022. p. 63–65.

19. Casem D. A model for a Kolsky bar experiment: application to experiment design. DEVCOM Army Research Laboratory; 2022. Report No.: ARL-TR-9416.

20. Casem D, Retzlaff E. A Kolsky bar for high-rate indentation. Journal of Dynamic Behavior of Materials. 2023; submitted.

21. Si B, Li Z, Xiao G, Shu X. Determination of mechanical properties from sharp dynamic indentation. Journal of Strain Analysis for Engineering Design. 2022;57:607–613.

22. Casem D, Grunschel S, Schuster B. Normal and transverse displacement interferometers applied to small diameter Kolsky bars. Experimental Mechanics. 2012;52:173–184.

23. Johnson G, Cook W. A constitutive model and data for materials subjected to large strains, high strain rates, and high temperatures. In: Proceedings of the 7th International Symposium on Ballistics; p. 541–547.

24. Simo J, Hughes T. Computational inelasticity. Springer-Verlag; 1998.

25. Armstrong R. On size effects in polycrystal plasticity. Journal of the Mechanics and Physics of Solids. 1961;9:196–199.

26. Abu Al-Rub R, Voyiadjis G. Analytical and experimental determination of the material intrinsic length scale of strain gradient plasticity theory from micro-and nano-indentation experiments. International Journal of Plasticity. 2004;20:1139–1182.

27. Voyiadjis G, Yaghoobi M. Review of nanoindentation size effect: experiments and atomistic simulation. Crystals. 2017;7:321.

28. Clayton J, Casem D, Lloyd J, Retzlaff E. Toward material property extraction from dynamic spherical indentation experiments. US Army Research Laboratory; 2022. Report No.: ARL-TR-9520.

29. Clayton J, Casem D, Lloyd J, Retzlaff E. Toward material property extraction from dynamic spherical indentation experiments on hardening polycrystalline metals. Metals. 2023;13:276.

30. Buckingham E. On physically similar systems; illustrations of the use of dimensional equations. Physical Review. 1914;4:345–376.

31. Sedov L. Similarity and dimensional methods in mechanics. Academic Press; 1959.

32. Cheng YT, Cheng CM. Scaling, dimensional analysis, and indentation measurements. Materials Science and Engineering R. 2004;44:91–149.

33. Ni W, Cheng YT, Cheng CM, Grummon D. An energy-based method for analyzing instrumented spherical indentation experiments. Journal of Materials Research. 2004;19:149–157.

34. Clayton J. Penetration resistance of armor ceramics: dimensional analysis and property correlations. International Journal of Impact Engineering. 2015;85:124–131.

35. Nguyen NV, Kim J, Kim SE. Methodology to extract constitutive equation at a strain rate level from indentation curves. International Journal of Mechanical Sciences. 2019;152:363–377.

36. Burley M, Campbell J, Dean J, Clyne T. Johnson-Cook parameter evaluation from ballistic impact data via iterative FEM modelling. International Journal of Impact Engineering. 2018;112:180–192.

37. Sasso M, Newaz G, Amodio D. Material characterization at high strain rate by Hopkinson bar tests and finite element optimization. Materials Science and Engineering A. 2008;487:289–300.

38. Sedighi M, Khandaei M, Shokrollahi H. An approach in parametric identification of high strain rate constitutive model using Hopkinson pressure bar test results. Materials Science and Engineering A. 2010;527:3521–3528.

39. Nguyen NV, Pham TH, Kim SE. Strain rate-dependent behaviors of mechanical properties of structural steel investigated using indentation and finite element analysis. Mechanics of Materials. 2019;137:103089.

40. Noble C, Anderson A, Barton et al. N. ALE3D: An arbitrary Lagrangian-Eulerian multi-physics code. Lawrence Livermore National Laboratory (LLNL); 2017. Report No.: LLNL-TR-732040.

41. Lesuer D, Kay G, LeBlanc M. Modeling large-strain, high-rate deformation in metals. Lawrence Livermore National Laboratory; 2001. Report No.: UCRL-JC-134118.

42. Zhu D, Mobasher B, Rajan S, Peralta P. Characterization of dynamic tensile testing using aluminum alloy 6061-T6 at intermediate strain rates. ASCE Journal of Engineering Mechanics. 2011;137:669–679.

43. Wu B, Cao Y, Zhao J, Ding W. The effect of superimposed ultrasonic vibration on tensile behavior of 6061-T6 aluminum alloy. International Journal of Advanced Manufacturing Technology. 2021;116:1843–1854.

44. Lu L, Dao M, Kumar P, Ramamurty U, Karniadakis G, Suresh S. Extraction of mechanical properties of materials through deep learning from instrumented indentation. Proceedings of the National Academy of Sciences. 2020;117:7052–7062.

45. Cao YP, Lu J. A new method to extract the plastic properties of metal materials from an instrumented spherical indentation loading curve. Acta Materialia. 2004;52:4023–4032.

46. Liu L, Ogasawara N, Chiba N, Chen X. Can indentation technique measure unique elastoplastic properties. Journal of Materials Research. 2009;24:784–800.

47. Clayton J, Lloyd J, Casem D. Simulation and dimensional analysis of instrumented dynamic spherical indentation of ductile metals. International Journal of Mechanical Sciences. 2023;251:108333.

48. Weaver J, Khosravani A, Castillo A, Kalidindi S. High throughput exploration of process-property linkages in Al-6061 using instrumented spherical microindentation and microstructurally graded samples. Integrating Materials and Manufacturing Innovation. 2016;5:192–211.

49. Oliver W, Pharr G. An improved technique for determining hardness and elastic modulus using load and displacement sensing indentation experiments. Journal of Materials Research. 1992;7:1564–1583.

50. Field J, Swain M. A simple predictive model for spherical indentation. Journal of Materials Research. 1993;8:297–306.

51. Johnson K. The correlation of indentation experiments. Journal of the Mechanics and Physics of Solids. 1970;18:115–126.

52. Donohue B, Ambrus A, Kalidindi S. Critical evaluation of the indentation data analyses methods for the extraction of isotropic uniaxial mechanical properties using finite element models. Acta Materialia. 2012;60:3943–3952.

53. Patel D, Kalidindi S. Correlation of spherical nanoindentation stress-strain curves to simple compression stress-strain curves for elastic-plastic isotropic materials using finite element models. Acta Materialia. 2016;112:295–302.

54. Chen G, Zhang X, Zhong J, Shi J, Wang Q, Guan K. New inverse method for determining uniaxial flow properties by spherical indentation test. Chinese Journal of Mechanical Engineering. 2021;34:94.

55. Clayton J. Nonlinear elastic and inelastic models for shock compression of crystalline solids. Springer; 2019.

56. Clayton J. Nonlinear mechanics of crystals. Springer; 2011.

57. Rosakis P, Rosakis A, Ravichandran G, Hodowany J. A thermodynamic internal variable model for the partition of plastic work into heat and stored energy in metals. Journal of the Mechanics and Physics of Solids. 2000;48:581–607.

58. Clayton J. Dynamic plasticity and fracture in high density polycrystals: constitutive modeling and numerical simulation. Journal of the Mechanics and Physics of Solids. 2005;53:261–301.

59. Francis H. Phenomenological analysis of plastic spherical indentation. Journal of Engineering Materials and Technology. 1976;98:272–281.

60. Matthews J. Indentation hardness and hot pressing. Acta Metallurgica. 1980;28:311–318.

61. Tabor D. The hardness of metals. Oxford University Press; 1951.

62. Hill R, Storåkers B, Zdunek A. A theoretical study of the Brinell hardness test. Proceedings of the Royal Society of London A. 1989;423:301–330.

63. Ito K, Arai M. Expanding cavity model combined with Johnson-Cook constitutive equation for the dynamic indentation problem. Journal of Engineering Materials and Technology. 2020;142:021005.

64. Nicholas T. Tensile testing of materials at high rates of strain: An experimental technique is developed for testing materials at strain rates up to 10^3 s^{-1} in tension using a modification of the split Hopkinson bar or Kolsky apparatus. Experimental Mechanics. 1981;21:177–185.

65. Arizzi F, Rizzi E. Elastoplastic parameter identification by simulation of static and dynamic indentation tests. Modelling and Simulation in Materials Science and Engineering. 2014;22:035017.

66. Phadikar J, Bogetti T, Karlsson A. Aspects of experimental errors and data reduction schemes from spherical indentation of isotropic materials. Journal of Engineering Materials and Technology. 2014;136:031005.

67. Dean J, Clyne T. Extraction of plasticity parameters from a single test using a spherical indenter and FEM modelling. Mechanics of Materials. 2017;105:112–122.

68. Zhang T, Wang S, Wang W. An energy-based method for flow property determination from a single-cycle spherical indentation test (SIT). International Journal of Mechanical Sciences. 2020;171:105369.

69. Wang M, Wang W. An inverse method for measuring elastoplastic properties of metallic materials using Bayesian model and residual imprint from spherical indentation. Materials. 2021;14:7105.

70. Clayton J, Lloyd J. A dynamic finite-deformation constitutive model for steels undergoing slip, twinning, and phase changes. Journal of Dynamic Behavior of Materials. 2021;7:217–247.

71. Zerilli F, Armstrong R. Dislocation-mechanics-based constitutive relations for material dynamics calculations. Journal of Applied Physics. 1987;61:1816–1825.

72. Preston D, Tonks D, Wallace D. Model of plastic deformation for extreme loading conditions. Journal of Applied Physics. 2003;93:211–220.

73. Zubelewicz A. Metal behavior at extreme loading rates: thermodynamics. Physical Review B. 2008;77(21):214111.

74. Voyiadjis G, Almasri A. A physically based constitutive model for fcc metals with applications to dynamic hardness. Mechanics of Materials. 2008;40:549–563.

75. Zubelewicz A. Mechanisms-based transitional viscoplasticity. Crystals. 2020;10:212.

76. Tirupataiah Y, Sundararajan G. A dynamic indentation technique for the characterization of the high strain rate plastic flow behaviour of ductile metals and alloys. Journal of the Mechanics and Physics of Solids. 1991;39:243–271.

77. Zhao M, Ogasawara N, Chiba N, Chen X. A new approach to measure the elastic–plastic properties of bulk materials using spherical indentation. Acta Materialia. 2006;54:23–32.

78. Savvatimskiy A. Measurements of the melting point of graphite and the properties of liquid carbon (a review for 1963–2003). Carbon. 2005;43:1115–1142.

79. D'Amelia R, Stracuzzi V, Nirode W. Introduction of differential scanning calorimetry in a general chemistry laboratory course: determination of heat capacity of metals and demonstration of the law of Dulong and Petit. Journal of Chemical Education. 2008;85:109–111.

80. Spierings A, Schneider M, Eggenberger R. Comparison of density measurement techniques for additive manufactured metallic parts. Rapid Prototyping Journal. 2011;17:380–386.

81. Reynolds M. The determination of the elastic constants of metals by the ultrasonic pulse technique. Knolls Atomic Power Laboratory; 1952. Report No.: AECU-1894.

Appendix. Higher Indentation Velocities

Additional simulations were performed to examine effects of a wider range of indentation rates. Velocity history input conditions of Fig. 2a for tests 2 and 3 were multiplied by a factor of 0.5, 2, 5, or 10, holding the time scale fixed. Predicted load-depth curves are shown in Fig. A-1.

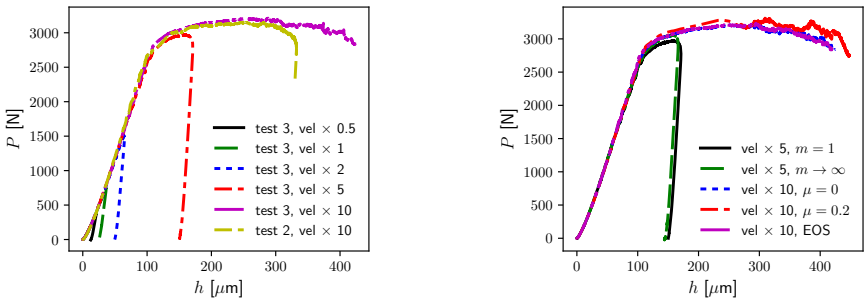

(a) baseline properties (b) variable properties

Fig. A-1 Indentation force P vs. depth h from simulations of of tests 2 and 3 with amplified input velocities: (a) baseline material properties of Table 2; 0.5, 2, 5$\times$ or 10$\times$ velocity increase for test 2 or test 3; (b) baseline properties vs. no thermal softening ($m \to \infty$), static and dynamic friction ($\mu = 0.2$), or equation of state (EOS) for thermal expansion and compressibility; 5$\times$ or 10$\times$ velocity increase for test 3. At 5–10$\times$ input velocities, thermal softening m and contact friction μ have significant influence, and nonlinear EOS rather than linear elasticity has modest influence.

Reduction of the input velocity by factor of 0.5 for test 3 produced a shallower indentation depth and a lower plastic strain than the original test 3. Differences in curvature of the load-depth response in Fig. A-1a are too small to enable resolution of strain rate effects between these two cases, since halving the strain rate produces only a 2–3% decrease in flow stress for the Johnson-Cook model with $C \approx 0.05$. Thus, further experiments with lower input velocities are likely not useful, since rate effects cannot be discerned and the plastic strain itself becomes too small to improve extraction of hardening parameters. Increasing the velocity by a factor of 2 produces an increase of the maximum indentation depth, and the maximum load is doubled to around 1500 N. However, the curvature of the $P - h$ response is nearly indistinguishable from that for the original test 3 (as expected given the low value of C). Experiments with the indentation rate multiplied by only a factor of two are not expected to provide much more information on material properties.

Increasing the input velocities by higher factors of 5 to 10 produces more drastic differences. Recall from Fig. 1 that the radius of the cylindrical output bar onto which the truncated indenter tip is machined is 0.794 mm, much smaller than the

radius of curvature of the indenter R of 3.175 mm. Thus, for sufficiently deep indentation, the sharp edge of the cylinder, where the spherical tip is truncated, will contact and penetrate the specimen. In this situation, the problem is no longer one of spherical indentation, but rather is a cylindrical punch with a slightly rounded front face. In the present dynamic regime, it is akin to ballistic penetration by a long rod. Results cannot be reasonably compared with static or lower-rate indentation since physical mechanisms differ.

As shown in Fig. A-2, this ballistic penetration regime is entered for a velocity increase of $5\times$ for test 3. In Fig. A-2a, localized plastic deformation of large magnitude arises at the edge of the cylinder as it penetrates the specimen. Adiabatic heating occurs simultaneously as shown in Fig. A-2b. For the $5\times$ amplification factor, the $P - h$ curve is rounded in Fig. A-1a, but the load eventually relaxes. From Fig. A-1a, the depth at which contact penetration begins is $h \approx 100\,\mu$m.

Also as shown in Fig. A-2, for a velocity increase of $10\times$ that for test 3, deformation is even more severe, and the local temperature rise much greater. The substrate thermal softens and approaches melt conditions in adiabatic shear zones at the contact interface along the cylinder wall. Elements become highly distorted, and the simulation terminates before elastic recovery can take place, if at all. The cylindrical bar with spherical tip is thus lodged in the substrate. For this highest velocity, plastic yielding of the steel input bar is predicted in the vicinity of the applied loading (i.e., due to impact from the striker bar). A similar undesirable situation occurs for a $10\times$ increase of velocity for test 2, as evident by the plateau in P versus h response in Fig. A-1a.

Results in Fig. A-1a use baseline material properties for the Al 6061-T6 material, with linear elasticity, no thermoelastic coupling, and no contact friction. Results in Fig. A-1b consider variations of these properties. Disabling thermal softening by setting $m \to \infty$ produces an increase in stiffness evident in the $P - h$ response at $5\times$ and $10\times$ input velocities. Thus, thermal softening becomes important in this higher-velocity regime, in contrast to the milder conditions considered in Section 4 and Fig. 11a. The friction coefficient μ also more noticeably affects the $P - h$ response at higher velocities, whereas use of $\mu = 0$ or $\mu = 0.2$ did not appreciably affect the $P - h$ response for lower rates of Sections 3 and 4.

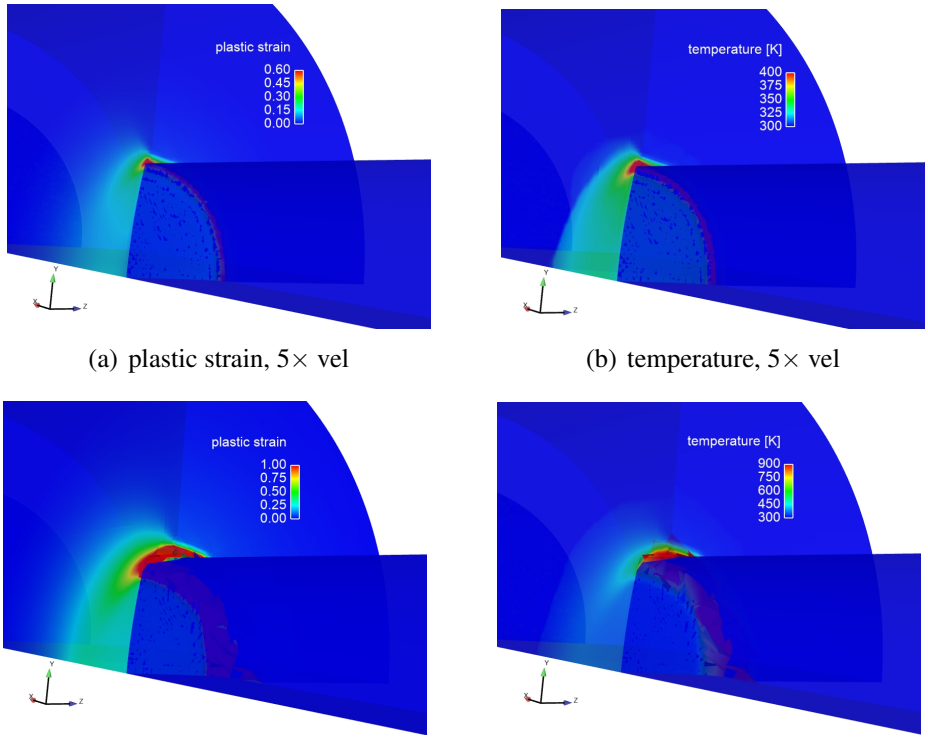

(a) plastic strain, 5× vel

(b) temperature, 5× vel

(c) plastic strain, 10× vel

(d) temperature, 10× vel

Fig. A-2 Contours of field variables from simulations of test 3 with amplified input velocity, $t = 40\,\mu$s: (a) effective plastic strain ϵ^P, 5× velocity increase, (b) absolute temperature T, 5× velocity increase, (c) effective plastic strain ϵ^P, 10× velocity increase, and (d) absolute temperature T, 10× velocity increase. In both cases (5 and 10× velocity), the cylindrical edge of the indenter penetrates the specimen, leading to strain localization and adiabatic heating, invalidating the test. Localized melting is approached and plastic deformation of steel input bar occurs for 10× velocity.

A pressure-volume-temperature equation of state (EOS)[1] is implemented in another simulation, with Grünesien parameter of 2.19 for thermoelastic coupling and pressure derivative of the bulk modulus of 4.42 from the experimental literature[2] for nonlinear compressibility. Use of the EOS influences results for $10\times$ velocity, but not by much until well after the penetration regime begins. Recall from Section 3.2 that adiabatic conditions are used in simulations, so heat conduction is ignored at time scales on the order of μs, a typical assumption[3,4], though some more rigorous FE studies consider conduction[5,6]. The presently predicted temperature rise is thus an upper bound with the Taylor-Quinney factor set to the default value of unity. Aluminum has a large thermal conductivity compared to many materials (e.g., steel), so any overestimation of temperature rise would be more severe in Al than in other, less conductive, materials.

The present results provide useful bounds on experimental loading protocols. The duration of the loading pulse is dictated by the time required for a longitudinal wave to traverse twice the length of the striker bar, which is considered fixed in the experimental setup. Variations in loading rate by a factor of 2 do not provide enough differences to discern strain rate sensitivity when C is small as for the present alloy. Much lower average input velocities than 1 m/s will produce too shallow indentations, with too little plastic strain, to improve determination of Johnson-Cook parameters. Increasing the input velocity by a factor between 2 and 5 leads to contact of the substrate with the cylindrical edge of the indenter-output bar interface, which invalidates the spherical indentation assumption. The experiment becomes ballistic impact and penetration by a rod for average input velocities exceeding 10 m/s. In this ballistic penetration regime, effects of thermal softening, rate sensitivity, static

[1]Clayton J. Nonlinear elastic and inelastic models for shock compression of crystalline solids. Springer; 2019.

[2]Guinan M, Steinberg D. Pressure and temperature derivatives of the isotropic polycrystalline shear modulus for 65 elements. Journal of the Physics and Chemistry of Solids. 1974;35:1501–1512.

[3]Lesuer D, Kay G, LeBlanc M. Modeling large-strain, high-rate deformation in metals. Lawrence Livermore National Laboratory; 2001. Report No.: UCRLJC-134118.

[4]Zhu D, Mobasher B, Rajan S, Peralta P. Characterization of dynamic tensile testing using aluminum alloy 6061-T6 at intermediate strain rates. ASCE Journal of Engineering Mechanics. 2011;137:669–679.

[5]Burley M, Campbell J, Dean J, Clyne T. Johnson-Cook parameter evaluation from ballistic impact data via iterative FEM modelling. International Journal of Impact Engineering. 2018;112:180–192.

[6]Ito K, Arai M. Simple estimation method for strain rate sensitivity based on the difference between the indentation sizes formed by spherical-shaped impactors. International Journal of Mechanical Sciences. 2021;189:106007.

and dynamic friction, thermal expansion, and nonlinear compressibility become increasingly important. The melt temperature can even be approached in adiabatic shear bands. The yield stress of other (steel) components of the system is exceeded in the ballistic regime (e.g., peak input velocities around 20 m/s), which will lead to permanent damage of the experimental device. So increasing the input velocity above a factor of around 2 is not recommended.

List of Symbols, Abbreviations, and Acronyms

TERMS:

Al	aluminum
ARL	Army Research Laboratory
CSM	continuous stiffness measurement
DEVCOM	US Army Combat Capabilities Development Command
FE	finite element
SHPB	split Hopkinson pressure bar
WC	tungsten carbide

MATHEMATICAL SYMBOLS:

a	contact radius
A	initial yield stress
B	strain hardening coefficient
C	strain rate sensitivity
E	elastic modulus
h	indentation depth
m	thermal softening exponent
n	strain hardening exponent
p	mean pressure
P	indentation force
R	indenter radius
t	time
T	temperature
W	indentation work
ϵ	strain

ν	Poisson's ratio
ρ	mass density
σ	stress
υ	velocity

1 (PDF) DEFENSE TECHNICAL INFORMATION CTR
DTIC OCA

1 (PDF) DEVCOM ARL
FCDD RLB CI
TECH LIB

1 (PDF) CALIFORNIA INST TECH
K BHATTACHARYA

1 (PDF) GEORGIA INST TECH
S KALIDINDI

1 (PDF) UNIV WISCONSIN
C BRONKHORST

1 (PDF) IOWA STATE UNIV
S PATHAK

2 (PDF) TEXAS A&M UNIV
G PHARR
K XIE

2 (PDF) JOHNS HOPKINS UNIV
L GRAHAM-BRADY
K RAMESH

1 (PDF) US NAVAL ACADEMY
E RETZLAFF

26 (PDF) DEVCOM ARL
FCDD RLA HC
J CRONE
J KNAP
FCDD RLA FR
M TSCHOPP
FCDD RLA
J CIEZAK
S SCHOENFELD
FCDD RLA B
R BECKER
A TONGE
FCDD RLA MB
J LIGDA
Z WILSON
FCDD RLA ME
J SWAB
L VARGAS-GONZALEZ
FCDD RLA MF
C HAINES
FCDD RLA T
M FERMEN-COKER
R FRANCART
FCDD RLA TB
D CASEM
J CLAYTON
P MCKEE
C MEREDITH
R REGUEIRO
S SATAPATHY
FCDD RLA TE
J LLOYD
T SCHARF
FCDD RLA TF
J CAZAMIAS
P JANNOTTI
R LEAVY
D MALLICK